MDPI

Article

Characteristics and Genetic Mechanism of Granite Weathering Crust of Songnan Low Uplift, Qiongdongnan Basin, South China Sea

Zhiyu Li [1,2,3]**, Jianhua Guo** [1,2,3] **and Shiqing Wu** [1,2,3,*]

[1] Key Laboratory of Metallogenic Prediction of Nonferrous Metals and Geological Environment Monitoring (Central South University), Ministry of Education, Central South University, Changsha 410083, China; lzy_kingsley@126.com (Z.L.); paper20240113@163.com (J.G.)
[2] Hunan Key Laboratory of Nonferrous Resources and Geological Hazards Exploration, Changsha 410083, China
[3] School of Geoscience and Info-Physics, Central South University, Changsha 410083, China
[*] Correspondence: wushiqing_123@126.com

Abstract: Recently, a large-scale gas reservoir was discovered in granitic buried hills of the Songnan Low Uplift in the Qiongdongnan Basin. However, the strong heterogeneity of granite reservoirs limits further exploration and evaluation. Based on observations of sixty core samples and sixty thin sections, mineral composition, zircon dating, apatite fission tracks, physical properties, image logs, outcrop surveys and seismic interpretations, the characteristics of granite weathering crust of the Songnan Low Uplift are analyzed, and its controlling factors and evolution process are evaluated. The results show that weathered granite in the study area can be divided into several zones, from top to bottom: eluvium–slope zone, sandy zone, weathered fracture zone and horizontal undercurrent vuggy zone. The reservoirs in the eluvium–slope zone are dominated by microfissures and intergranular dissolution pores and have an average porosity of 4.68% and permeability of 2.34 md; the reservoirs in the sandy zone are composed of intergranular and intragranular dissolution pores and have an average porosity of 11.46% and permeability of 4.99 md; the reservoirs in the weathered fracture zone consist of various fractures and have an average porosity of 3.91% and permeability of 2.5 md; the reservoirs in the horizontal undercurrent vuggy zone are subhorizontal fractures and vugs and have an average porosity of 2.7% and permeability of 0.23 md. The development of granite reservoirs is jointly influenced by petrology and minerals, long-term exposure in a warm humid paleoclimate, faults, diverse topographies and shallow buried depth. Based on the above, our study establishes a development model of weathering crust and suggests that only the gentle slope and platform remain strongly weathered zones. After undergoing a complex evolution process of formation–destruction/denudation–regeneration–preservation, the current weathering crust of the Songnan Low Uplift is finally established. The results of this study have important theoretical and application value for the hydrocarbon exploration of buried hills in the Qiongdongnan Basin and provide a reference example for other granite reservoirs worldwide.

Keywords: Songnan Low Uplift; granite; core samples; zircon dating; weathering crust; zonation; genetic mechanism; evolution

1. Introduction

As a kind of dense and hard rock, granite lacks primary pores and reasonable permeability and generally does not provide accumulation conditions for an effective oil and gas reservoir. However, the physical properties of granite could be greatly improved after modification by dissolution and faulting, and the reservoir spaces formed are mainly secondary dissolution pores and fractures [1–3]. So far, some granitic buried hills have already achieved significant exploration and development results. The Bach Ho oilfield in

Vietnam has produced approximately one billion barrels of crude oil and 3×10^8 m^3 natural gas from fractured granite [4,5]. The Kharir oilfield in Yemen contains proven geological petroleum reserves of over 1×10^8 tons, with production from a single well reaching up to 300–400 t/day [6]. The average productivity of pre-Cambrian granite rocks in the Bongor Basin has been more than 300 m^3/day since 2012 [7]. The Penglai oilfield in the Bohai Bay Basin is the largest granite reservoir in China, with an oil-bearing area of 80.2 km^2 and more than 2×10^8 tons of reserves [8–10]. In addition, the Paleoproterozoic granite of the JZ25-1S oil and gas field in Liaodong Bay also contains about 9×10^7 m^3 of hydrocarbons [6,11]. These figures indicate that the exploration potential of granite reservoirs is great.

To date, many scientists have carried out extensive works on granite weathering crust reservoirs. Vertical zonation of the weathering crust is determined based on weathering intensity indices such as granite color, rock structure, mineral composition, logging characteristics, reservoir space types and geochemical indicators [8–10,12–19]. There are also various geological models of weathering crust established in previous studies [9,10,16,20–22]. Moreover, the formation of weathering crust differs in different areas. For example, some studies propose that mechanical breakdown and chemical weathering play crucial roles in the formation of granite reservoirs [16,20], while other studies suggest that the top of altered granite contributes little to oil and gas production and fracture layers related to the decompression of granitic batholith or/and large deep faults are the main storage spaces [5,23,24]. Huang et al. (2016) and Wei et al. (2018) emphasized the influence of topography on the preservation and differential evolution of weathering crust reservoirs [25,26].

However, previous studies mainly focused on the current vertical structures of weathering crust reservoirs without characterizing their multistage development in geological evolution. In fact, the granite weathering crust has undergone a complicated process of weathering and erosion over the long history of uplift and subsidence of the basement. Wang (2015) and Ye et al. (2020) indicated that the granite structure of Penglai oilfield went through two stages of slow uplift and subsidence and at least one stage of rapid uplift [8,22], and its erosion thickness is more than 2000 m, suggesting that it is difficult to preserve weathering crust reservoirs until the structure has been stabilized or covered. Without taking these factors into account, it is hard to predict the optimal locations of granite reservoirs.

Exploration of the Qiongdongnan Basin (QDNB) over the past two decades has focused on the Miocene central canyon oil and gas belt and Oligocene reef limestone and sandy conglomerates [27–32], while little attention has been paid to buried-hill reservoirs [21,33,34]. The amount of research on granite reservoirs in the QDNB is much less compared to those mentioned above [35,36]. Recent drillings of the Songnan Low Uplift (SNLU) show that the thickness of the Mesozoic granite reservoir is more than 100 m and the natural gas reserves amount to more than 1×10^8 m^3, indicating huge exploration potential [37]. Therefore, systematic research on the characteristics and genetic mechanism of granite reservoirs and their distribution is urgently needed for further exploration and development. Taking the SNLU as an example, we utilized drill cores, thin sections, physical properties, image logging, outcrop and seismic data to reclassify the vertical zonation of its granite weathering crust and analyzed the genetic mechanism of the weathering crust; then, we characterized its multistage evolution from a dynamic perspective based on zircon dating data and apatite fission track modeling. These results provide not only a significant supplement to the understanding of weathering crust reservoirs in the QDNB but also crucial guidance to hydrocarbon exploration activities in granitic rocks around the world.

2. Geological Setting

The QDNB is a Cenozoic passive continental margin fault basin with a pre-Tertiary basement located in the northern region of the South China Sea [38]. It has a NE-SW trend and covers an area of about 6×10^4 km^2. Most of these formations are located in deep-water areas (water depth over 300 m). The SNLU lies in the middle of a deep-water area that is bounded on the north by Songnan-Baodao Sag, on the west by Lingshui Sag,

on the south by Beijiao Sag and on the east by Changchang Sag (Figure 1). This nearly EW-trending uplift covers an area of 2950 km^2 with a northern faulted slope and a southern gentle margin [29,39,40].
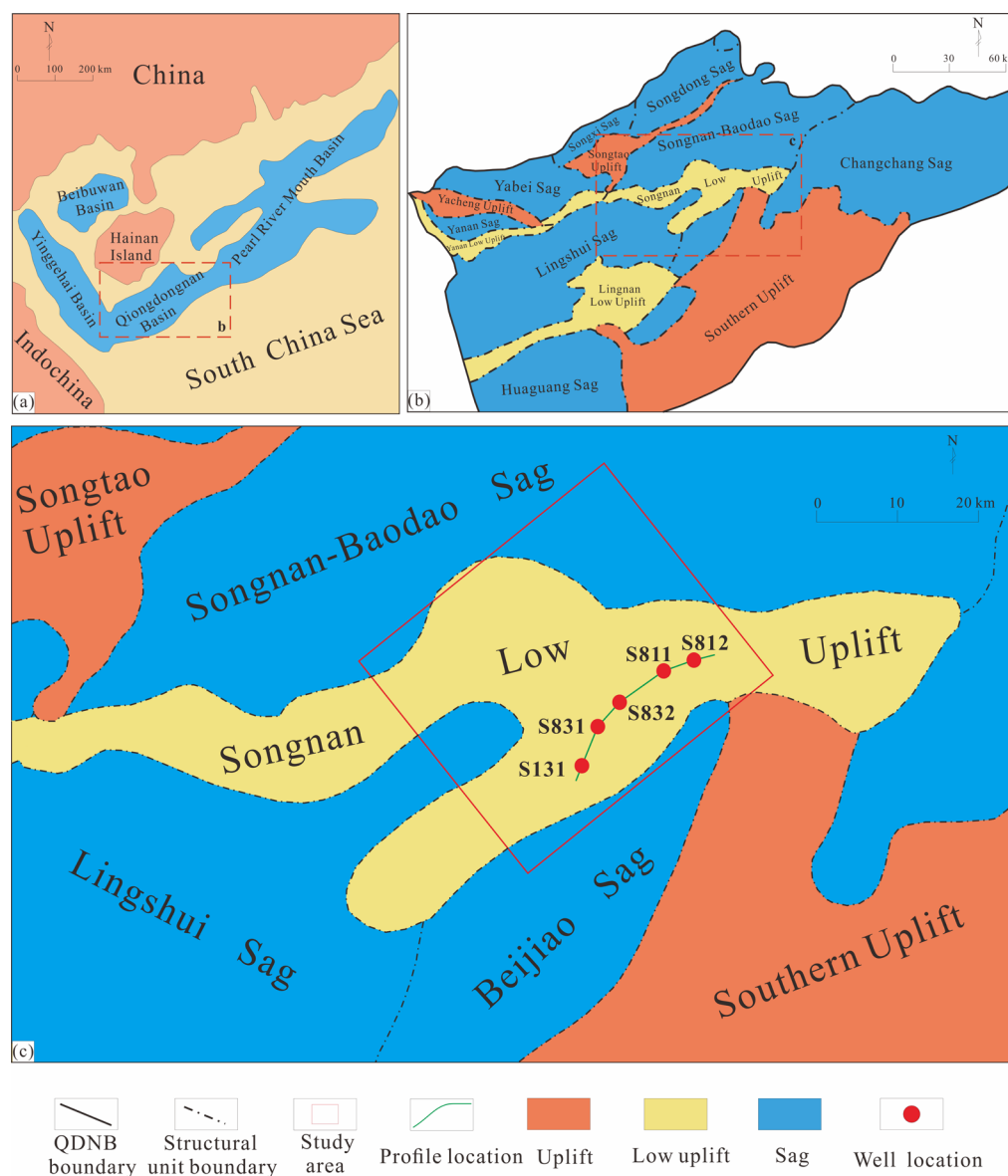

Figure 1. (**a**) Sketch map showing location of Qiongdongnan Basin in South China Sea. (**b**) Tectonic units of Qiongdongnan Basin (modified after Zhou et al. [40]); (**c**) location of Songnan Low Uplift.

Multistage tectono-magmatism movements made the SNLU an exposed paleo-uplift until the Mesozoic granite basement was covered by clastic sediments of the Oligocene Yacheng and Lingshui formations. After the Miocene, the entire QDNB began to sink, and the study area was filled with marine mudstone of the Sanya, Meishan and Huangliu formations and bathyal–abyssal deposits of the Pliocene Yinggehai and Pleistocene Ledong formations (Figure 2). The littoral–neritic deposits of the Yacheng and Lingshui formations were the major source rocks, and the thick Neogene mudstone formed the sealed caps in the deep-water area of the QDNB [41,42].

The study area is surrounded by hydrocarbon-generating sags and has a prosperous source rock condition [29,30,43,44]. The average total organic carbon of the Yacheng formation in the Lingshui and Songnan-Baodao Sags is 1.37%, and the area of effective source rock (vitrinite reflectance more than 1.3%) can reach up to 4000 km^2 [41,45]. Multiple

fault belts and structural ridges around the SNLU make it a favorable area for hydrocarbon accumulation [32,33,46].
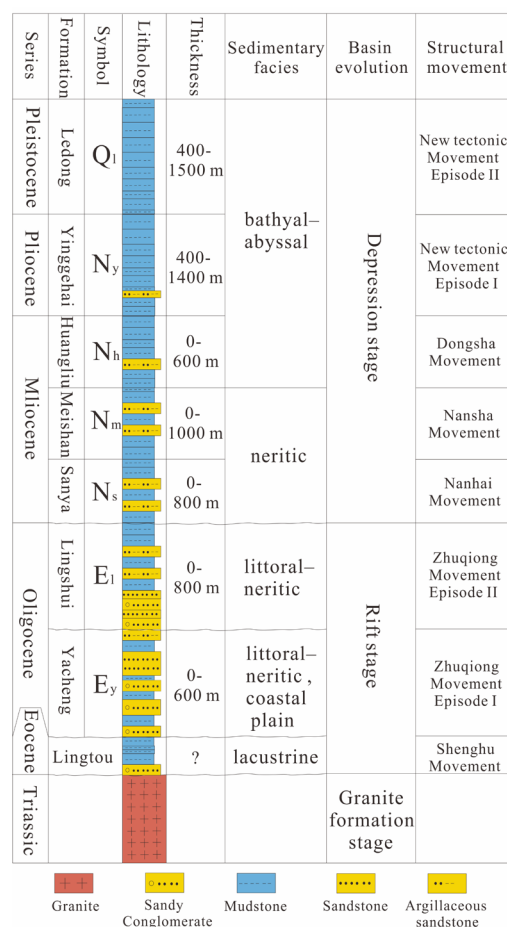
Figure 2. Comprehensive stratigraphic column showing sedimentary characteristics and major tectonic events in Songnan Low Uplift (modified after Yang et al. [32] and Zhou et al. [40]). Q, Quaternary; N, Neogene; E, Paleogene; The symbol "?" implies the Lingtou formation is undrilled in Songnan Low Uplift.

3. Materials and Analytical Methods

3.1. Materials

Core samples, thin sections, and image logging data from wells S131, S831, S832, S811 and S811 were collected at the Zhanjiang branch of the China National Offshore Oil Corporation (CNOOC). Data on zircon dating, apatite fission track, X-ray diffraction analysis, physical properties and palynofacies analysis from 5 wells as well as 3D seismic data covering the study area (approximately 2000 km^2) were also obtained from the Zhanjiang branch of the CNOOC (Table 1).

Table 1. Summary of data from wells in SNLU.

Data	Cores	Thin Sections	Zircon Dating	Apatite Fission Track	X-ray Diffraction Analysis	Image Logging	Physical Property	Palynofacies Analysis
Number of samples	60	60	4	5	30	5	58	20
Depth (m)	2853–3470	2853–3470	3000–3566	2660–3541	2963–3244	2863–3566	2980–3566	3050–3300
Lithology	granite	granite	granite	granite	granite	granite	granite	mudstone

A number of granite outcrops from Dawei Mountain of Liuyang were visited and photographed to better understand the macroscopic development and distribution characteristics of weathering crust reservoirs.

3.2. Analytical Methods

The following analyses were carried out at the laboratory of the Zhanjiang branch of the CNOOC:

Thin-section observations were performed using an optical petrographic microscope (Olympus BX41, manufactured by Olympus, Tokyo, Japan) with a digital camera (Olympus E420, manufactured by Olympus, Tokyo, Japan) mounted for image capture. The observations were carried out at 40× magnification under plane-polarized and cross-polarized light.

X-ray diffraction analysis was conducted, for which granite samples were crushed to particles of less than 100 mesh and dried. The analysis was carried out using an Ultima VI X-ray diffractometer (manufactured by Rigaku, Tokyo, Japan). Experimental conditions included a voltage of 40 kV, current of 40 mA and scanning rate of 4°/min in the range of 3°–85°(2θ). All processes followed the Chinese Oil and Gas Industry Standard SY/T 5163–2010 [47].

Analysis of the physical properties of granite samples was performed with an automatic porosimeter and a super permeameter. The experiments were conducted following the criteria of GB/T 29172-2012 [48] and the process described by Zhang et al. [49].

SHRIMP zircon U–Pb dating was conducted at the Institute of Geomechanics, Chinese Academy of Geological Sciences. First, samples were crushed to 60–100 mesh size. After washing off the dust with water, the magnetic minerals, such as magnetite, were removed by magnetite, and then zircons were separated by heavy liquid. After that, zircons were selected under a binocular microscope. Then, zircons and the standard sample were adhered to the glass plate and cast with epoxy resin. After slicing and polishing, orthogonal polarization and cathode-luminescent photos of zircons were taken. Finally, U, Th and Pb isotope contents and zircon dating were determined through the ion probe SHRIMP-RG (manufactured by Thermo Fisher Scientific, Waltham, MA, USA). Data processing was carried out using the ISOPLOT program (version 4.15).

Apatite fission track (AFT) dating was completed at Zircon Technology Co., Ltd., Beijing. First, apatite particles were dripped with epoxy resin. After grinding and polishing, the inner surface of minerals was exposed. The samples were etched in 5.5 mol/L HNO_3 for 30 s at 21 °C to reveal spontaneous tracks. The glass standard CN5 [50] and the samples were put into a nuclear reactor for irradiation using low-uranium muscovite as the external detector. Then, the muscovite was etched with 40% HF at 25° for 20 s to reveal the induced fission tracks. The AUTOSCAN system (manufactured by Autoscan Systems Pty. Ltd., Melbourne, Australia) was used to measure fission track density and length. The age of the apatite grains was calculated using the zeta calibration method. Thermal history modeling was performed using the inverse Monte Carlo modeling approach in HeFTy 1.9.1 software based on the measured AFT lengths and ages.

Palynofacies analysis was carried out at the Nanjing Institute of Palaeontology. Samples were treated with HCl to remove calcium carbonate and then HF to remove silicon. Suspended substances were obtained after flotation by heavy liquid (specific gravity 2.20). After the obtained materials were washed and sliced, palynomorphs and palynomacerals were visualized with a Leica DM1000 microscope (manufactured by Leica, Frankfurt, Germany) using transmitted white light.

Geoframe software (version 4.3) was used to complete the well seismic calibration and seismic interpretation of the granite structure and calculate the variance cube attributes of seismic data.

4. Results

### *4.1. Petrological Characteristics*

4.1.1. Mineralogical Compositions

The results of X-ray diffraction analysis show that the petrology of the study area is dominated by monzonitic granite and granodiorite (Figure 3). Monzonitic granite is grayish red and light red with a massive structure (Figure 4a,b), and quartz, K-feldspar and plagioclase account for more than 80% of the mineral content, with content ranging from 30% to 40%, 20% to 40% and 20% to 30%, respectively (Table 2). The monzonitic granite also consists of approximately 10% clay and 2% mafic minerals (amphibole and biotite). Some calcite and pyrite may have formed from late hydrothermal processes. Granodiorite is gray and white (Figure 4c), mainly composed of plagioclase, quartz, K-feldspar, amphibole and biotite. The content of plagioclase is higher than that in monzonitic granite, reaching about 45%. The average content of quartz, K-feldspar, mafic minerals and calcite is 30%, 15%, 4% and 1%, respectively (Table 2). As the main mafic mineral, biotite can be observed in drill cores (Figure 4c).

Table 2. Mineral composition of granite in SNLU.

| Well	Depth (m)	Qz (wt%)	Kfs (wt%)	Pl (wt%)	Cl (wt%)	Cal (wt%)	Mf (wt%)	Total (wt%)	Fs (wt%)	Qz + Fs (wt%)
S811	2905	38	32	18	10	-	2	100	50	88
S811	2909	37	33	19	8	2	1	100	52	89
S811	2916	35	25	20	14	3	3	100	45	80
S811	2924	33	34	20	13	-	-	100	54	87
S811	2932	32	46	15	6	-	1	100	61	93
S811	2938	34	36	16	13	-	1	100	52	86
S811	2942	35	30	20	15	-	-	100	50	85
S811	2958	39	37	17	7	-	-	100	54	93
S811	2963	41	29	20	7	2	1	100	49	90
S811	2971	30	22	31	12	3	2	100	53	83
S811	2982	34	35	21	7	3	-	100	56	90
S811	2993	32	36	17	10	2	3	100	53	85
S811	3002	22	27	37	9	5	-	100	64	86
S811	3011	40	28	17	10	5	-	100	45	85
S811	3017	40	21	21	11	4	3	100	42	82
S811	3027	35	22	29	7	6	1	100	51	86
S811	3033	29	36	27	3	5	-	100	63	92
S811	3053	38	33	20	6	3	-	100	53	91
S811	3061	33	21	30	13	3	-	100	51	84
S811	3082	35	25	23	14	3	-	100	48	83
S131	2612	32	21	28	17	-	2	100	49	81
S131	2652	35	31	30	4	-	-	100	61	96
S832	3068	30	19	37	8	-	6	100	56	86
S832	3104	32	22	38	4	-	4	100	60	92
S832	3136	29	20	40	9	-	2	100	60	89
S832	3160	33	17	38	8	2	2	100	52	85
S832	3224	36	17	38	5	1	3	100	55	91
S832	3240	32	18	42	3	-	4	100	59	95
S832	3244	17	26	40	8	4	5	100	66	83
S832	3248	27	19	44	7	-	3	100	63	90

Qz, quartz; Kfs, K-feldspar; Pl, plagioclase; Cl, clay; Cal, calcite; Mf, mafic mineral; Fs, feldspar.
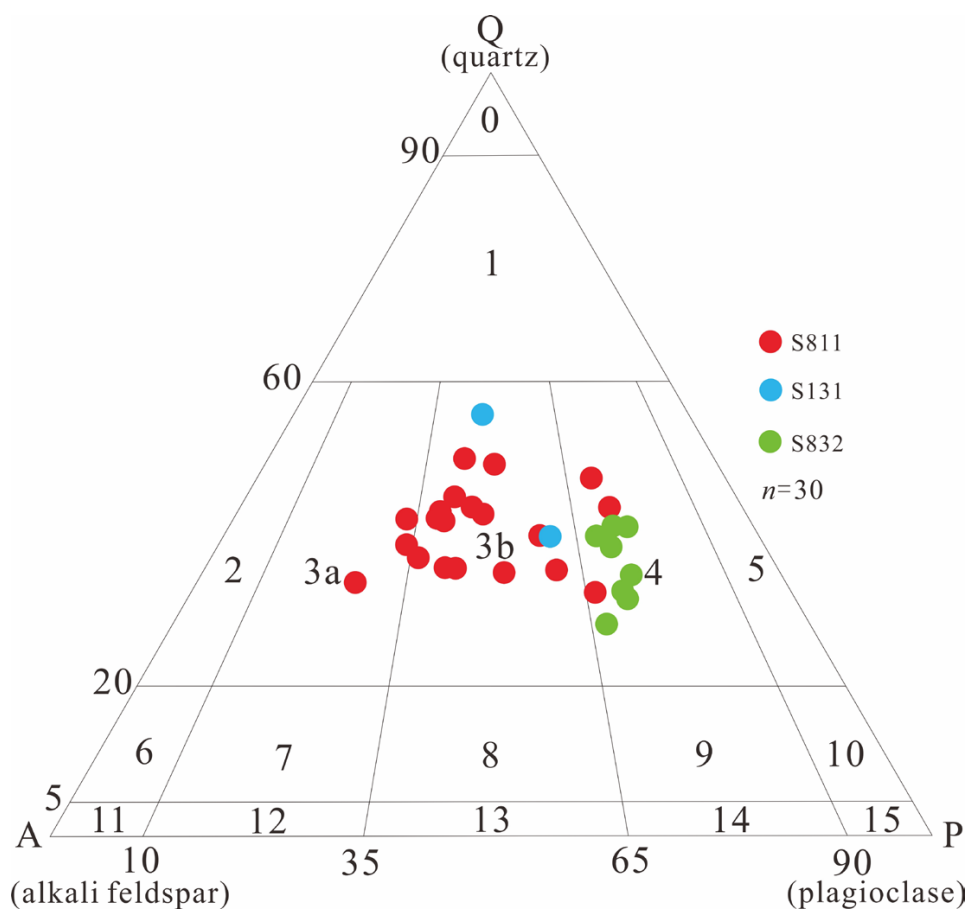
Figure 3. QAP diagram of granite from SNLU (modified after Ye et al. [18]): 0. quartzolite; 1. quartz-rich granitoids; 2. alkali feldspar granite; 3a. syenogranite; 3b. monzonitic granite; 4. granodiorite; 5. tonalite; 6. quartz alkali feldspar syenite; 7. quartz syenite; 8. quartz monzonite; 9. quartz monzodiorite, quartz monzogabbro; 10. quartz diorite, quartz gabbro, quartz anorthosite; 11. alkali feldspar syenite; 12. syenite; 13. monzonite; 14. monzodiorite, monzogabbro; 15. diorite, gabbro.

4.1.2. Core Characteristics

Observing core samples from five exploration wells, we found a loose mixed layer filled with poorly sorted mud-bearing sandy conglomerates and granite blocks on top of the granite weathering crust. Apparently, this is a residual product of the granite due to severe weathering and short-distance transport and is therefore called the eluvium and slope layer (Figure 4d,e). Massive granite disappears beneath the layer, and the rock is strongly dissolved into quartz grains, clay and gravels with a loose sandy structure (Figure 4f,g). As the dissolution decreases, the degree of consolidation of the rock improves and various fractures can be observed. Some weathered fractures are filled with clay (Figure 4h). Frequent high-angle cross-fractures occur in the upper part of the weathered fractured granite, while low-angle fractures and vugs caused by acidic fluid can be observed in the lower part. Some vugs are filled with calcite (Figure 4i). The granite cores from top to bottom have two obvious features: (i) differential weathering makes the cores of vertical granite structures perform differently, and (ii) weathering intensity decreases with increasing depth.
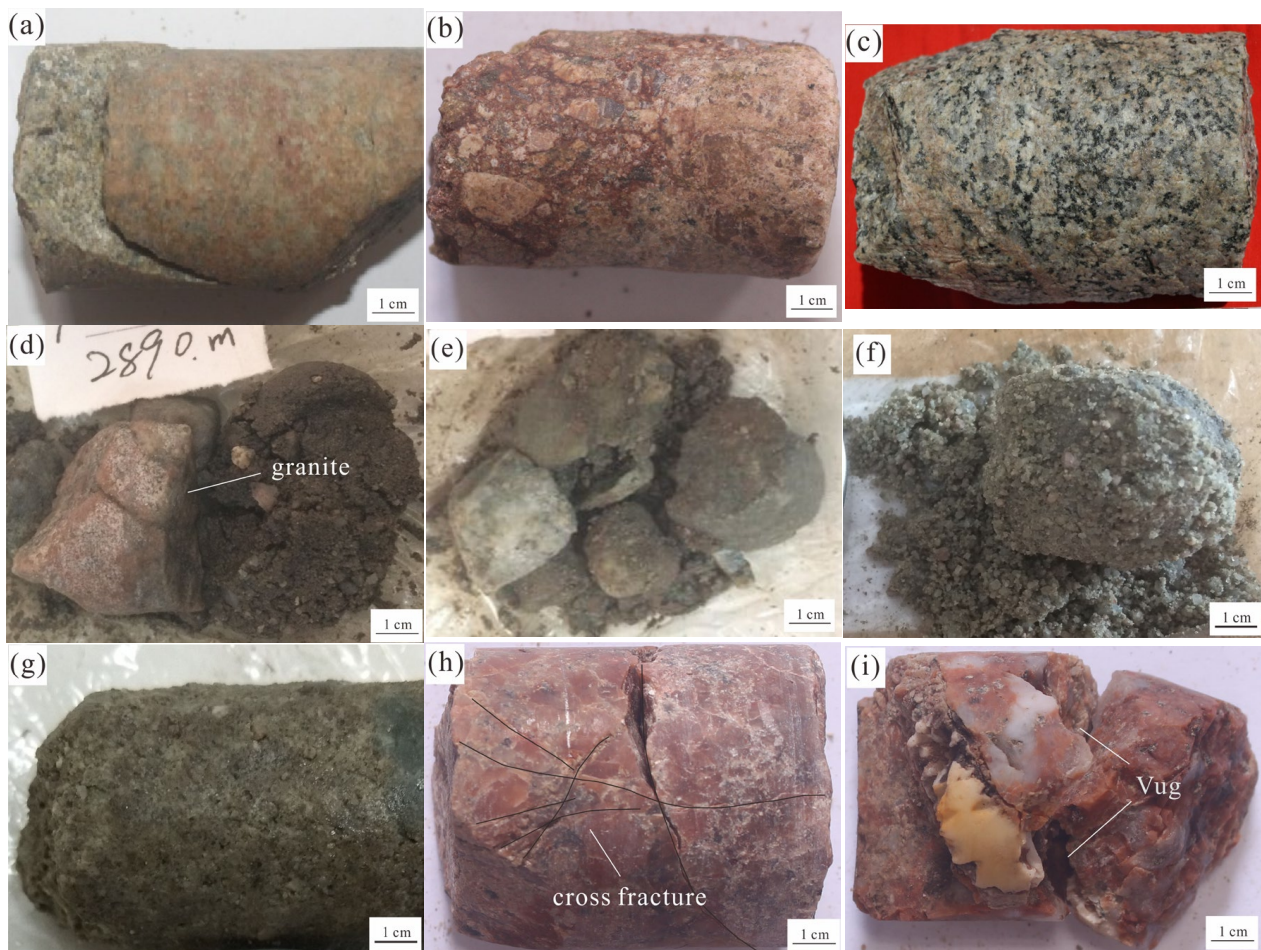
Figure 4. Granite cores of SNLU: (**a**) fractured monzonitic granite (well S831, 2860 m); (**b**) monzonitic granite with high content of K-feldspar (well S811, 2974 m); (**c**) granodiorite with high content of mafic mineral (well S832, 2970 m); (**d**) eluvial and slope layer, note massive granite (well S832, 2890 m); (**e**) mixture of weathered gravel, sandstone and clay (well S832, 2895 m); (**f**) weathered granite with loose sandy structure (well S832, 2905 m); (**g**) weathered granite with severe dissolution (well S832, 2935 m); (**h**) unfilled fractures and high-angle cross-fractures (well S812, 3361 m); (**i**) vugs filled by calcite, note dissolution deformation (well S812, 3470 m).

4.2. Chronological Characteristics

4.2.1. Zircon U-Pb Dating

The zircons from well S811 yielded 56 valid data points. All analysis points lie on or near the Concordia line and show good consistency (Figure 5a). The age of the zircon particles ranges from 201 to 285 Ma, with a weighted mean of 249 $\pm$ 10 Ma (MSWD = 2.1). The zircons from well S812 yielded 23 valid data points (Figure 5b). With the exception of one zircon grain with a ^{206}Pb/^{238}U age of 258 Ma, the remaining zircons are narrowly distributed along the Concordia line. The weighted mean ^{206}Pb/^{238}U age is calculated to be 242 $\pm$ 2.8 Ma (MSWD = 1.4). U–Pb dating was performed for 24 zircon particles from well S831, and concordant data were obtained for 21, with a weighted mean ^{206}Pb/^{238}U age of 229 $\pm$ 4.8 Ma (MSWD = 2.4) (Figure 5c). The zircons from well S832 yield 27 valid data points (Figure 5d). The age of the zircon particles ranges from 210 to 245 Ma, with a weighted mean of 225 $\pm$ 1.8 Ma (MSWD = 0.76). The results of zircon U–Pb dating indicate that the granite was crystallized in the Early to Middle Triassic.

4.2.2. Apatite Fission Track

The AFT ages and confined track length measurement from samples S811-03, S812-01, S831-01, S832-01 and S131-02 are shown in Table 3. The central age ranges from 17.3 ± 12 Ma to 29.0 ± 3 Ma. Samples S812-01 ($P(\chi^2) = 87.5\%$), S831-01 ($P(\chi^2) = 99.8\%$), S832-01 ($P(\chi^2) = 18.7\%$) and S131-02 ($P(\chi^2) = 44.1\%$) pass the $P(\chi^2)$ test ($P(\chi^2) \geq 5\%$), indicating that they were from a homogeneous cooling source. Sample S811-03 ($P(\chi^2) = 4.1\%$) fails the $P(\chi^2)$ test, reflecting heterogeneous age components (Table 3). Considering that all central or/and pooled ages of wells S811, S812, S831 and S832 are younger than the corresponding zircon ages, it is suspected that granite in the SNLU had undergone complete annealing behavior after crystallization.
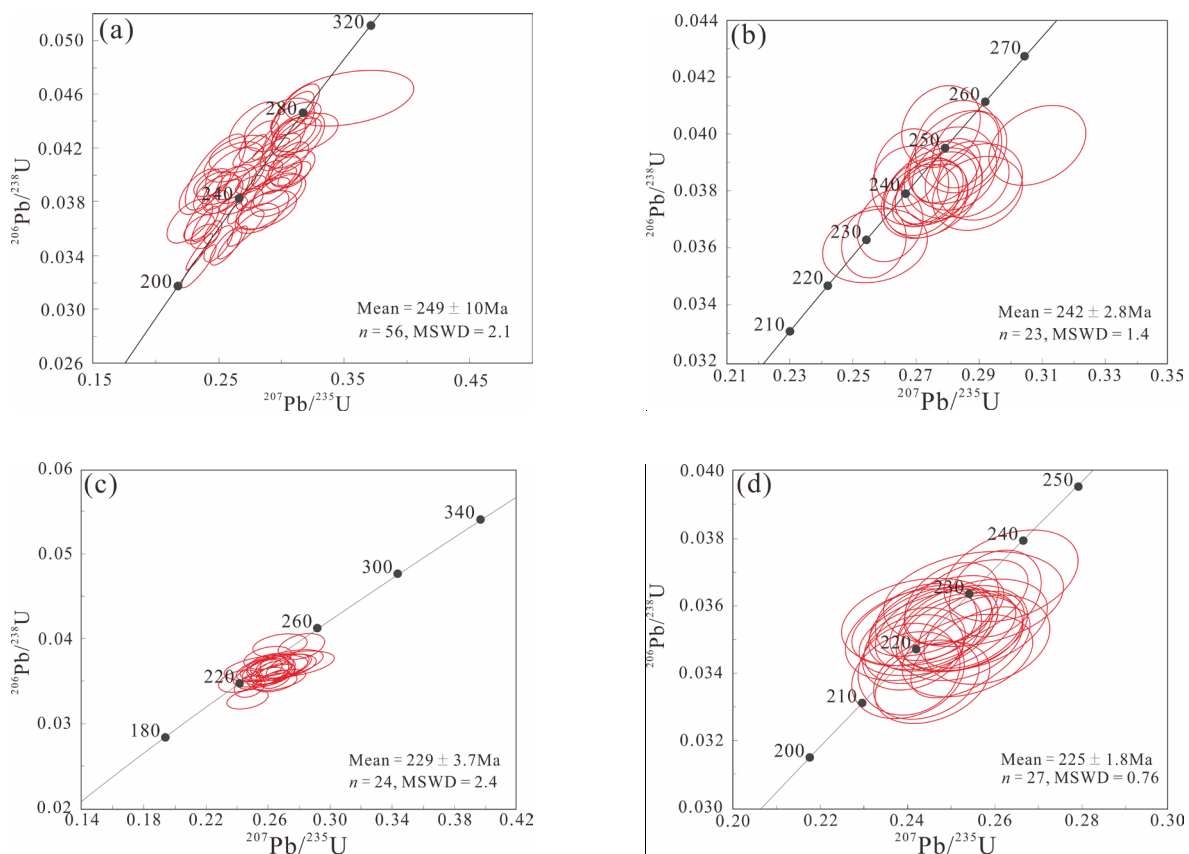
Figure 5. Concordia diagrams for zircon particles from granitic rocks in SNLU: (**a**) well S811; (**b**) well S812; (**c**) well S831; (**d**) well S832. Mean, mean zircon age; *n*, number of zircon particles; MSWD, mean square weighted deviation.

Table 3. Apatite fission track analytical results of granite samples from SNLU.

Sample ID	*n*	ρ_s $(10^5/cm^2)$	(N_s)	ρ_i $(10^5/cm^2)$	(N_i)	ρ_d $(10^5/cm^2)$	(N_d)	$P(\chi^2)$ (%)	Central Age $(\pm 1 \sigma)$ (Ma)	Pooled Age $(\pm 1 \sigma)$ (Ma)	MTL ± 1 σ (µm)	D_{par} (µm)
S811-03	43	2.48	355	16.83	2406	9.93	5323	4.1	29.0 ± 3	29.0 ± 2	11.4 ± 1.8	0.91
S812-01	21	2.01	417	16.78	3487	7.26	5323	87.5	26.5 ± 11	26.5 ± 11	8.77 ± 1.1	2.32
S831-01	42	1.25	316	8.36	2121	6.85	5323	99.8	20.0 ± 2	20.0 ± 2	12.1 ± 1.8	1.06
S832-02	130	1.7	93	12.98	712	6.65	5323	18.7	17.3 ± 12	17.3 ± 12	11.1 ± 1.7	1.36
S131-01	42	3.54	451	19.16	2444	9.73	5323	44.1	25.7 ± 3	25.7 ± 2	12.5 ± 1.8	1.44

n: number of dated apatite or zircon crystals; ρ_s (ρ_i): spontaneous (induced) track density; N_s (N_i): number of counted spontaneous (induced) tracks; ρ_d: dosimeter track density; N_d: number of tracks counted on dosimeter; $P(\chi^2)$: probability of obtaining chi-square value for *n* degrees of freedom; MTL, mean track length; D_{par}: average etch pit diameter of fission tracks.

*4.3. Reservoir Characteristics*

4.3.1. Thin-Section Characteristics

Thin-section observations show that the secondary storage spaces of weathering crust in the study area consist mainly of fractures and dissolution pores. Fractures are further divided into structural fractures, dissolution fractures and microfissures according to their shape, size and genesis. Dissolution pores include intragranular dissolution pores and intergranular dissolution pores.

Structural fractures are caused by complex tectonic stresses. They can extend far to cut quartz and feldspar particles (Figure 6a). Structural fractures are common in the granite of the study area and usually intersect to form network fractures. Some of them are filled or partially filled with calcite or clay (Figure 6b). Microfissures occur due to breakup and deformation caused by mechanical reworking or condensation and shrinkage of granite. They can provide essential channels for fluid seepage, and dissolution pores along fractures can be observed (Figure 6c). Dissolution fractures result from the leaching of acidic fluid along structural fractures and microfissures. Feldspar and biotite in granite are subject to hydrolysis and hydration, causing fracture surfaces to become irregularly enlarged and widened. Most dissolution fractures are semi-filled or unfilled (Figure 6d). Dissolution fractures significantly improve the physical properties of weathering crust reservoirs.

Dissolution pores in granite reservoirs are formed by the dissolution of feldspar, quartz and biotite. Intergranular dissolution pores mainly have a bead-like form and occur at the contact edges of various mineral particles (Figure 6e). They constitute the major storage spaces of strongly weathered granite. Intragranular dissolution pores are predominately developed in feldspar or quartz particles. They are micro-sized and vary in shape, which can improve the porosity of reservoirs to some extent (Figure 6f).
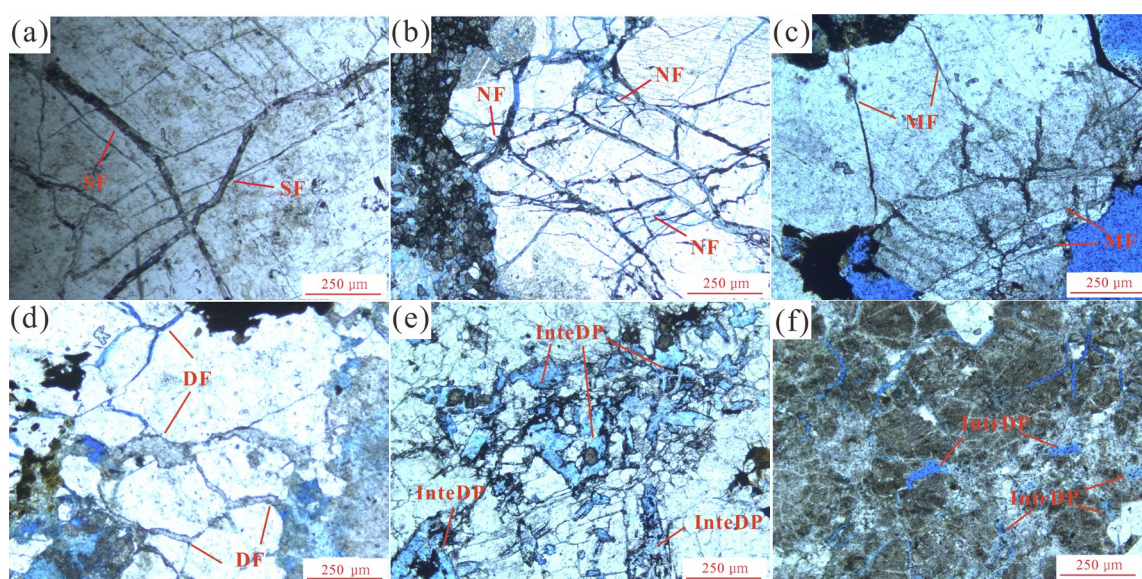

Figure 6. Thin sections of granite from SNLU: (**a**) structural fractures (well S831, 2860 m), plane-polarized light; (**b**) net-like fractures (well S811, 3347 m), plane-polarized light; (**c**) microfissures, note dissolution pores along fractures (well S811, 2952 m), plane-polarized light; (**d**) fractures widened by dissolution in feldspar (well S831, 2964.5 m), plane-polarized light; (**e**) intergranular dissolution pores between mineral particles (well S811, 2960.5 m), plane-polarized light; (**f**) intragranular dissolution pores in feldspar (well S811, 2968 m), plane-polarized light. SF, structural fracture; NF, network fracture; MF, microfissure; DF, dissolution fracture; InteDP, intergranular dissolution pore; IntrDP, intergranular dissolution pore.

4.3.2. Image Logging Characteristics

The FMI logs show that the section from 2920 to 2922 m in well S811 is dominated by dark conductive masses and irregular bright resistive spots. The dark conductive masses represent weathered clay, and the bright and highly resistive spots are residual weathered breccia and gravels, revealing the characteristics of strongly weathered granite reservoirs (Figure 7a). Fractures in the weathering crust reservoirs are well developed and are shown as dark sinusoidal curves in the image logs. They can be divided into three types according to the shape characteristics of sinusoidal curves: continuous fracture (CF), semi-continuous fracture (SCF) and widened fracture (WF). Continuous fractures mainly correspond to structural fractures and usually occur as parallel complete sinusoidal curves in groups (Figure 7b). Semi-continuous fractures are primarily diagenetic fractures; they are often caused by the condensation and shrinkage of magma and are characterized by incomplete arcs that do not extend throughout the wellbore (Figure 5c). Widened fractures represent dissolution fractures, which are shown as enhanced curves in the image; their surfaces are expanded by the dissolution of meteoric water and other acidic fluids (Figure 7d). Fresh granite is brighter and more resistive compared to weathered granite because it has fewer conductive fractures and weathered clay, suggesting weaker weathering intensity (Figure 7e).
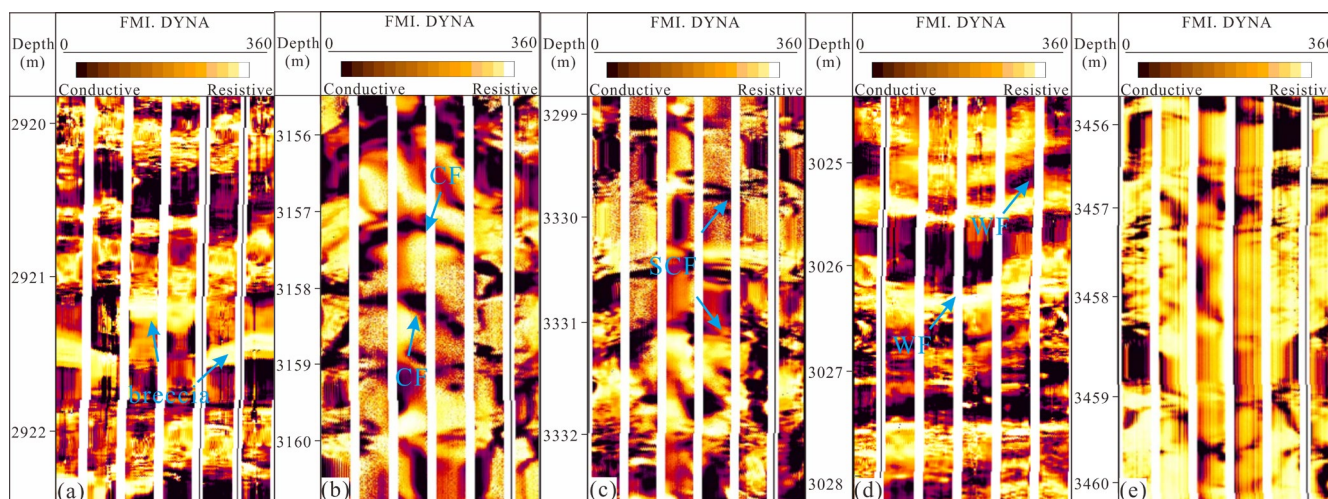

Figure 7. FMI log features of weathering crust reservoirs in study area: (**a**) strongly weathered granite, note bright massive breccia; (**b**) continuous fracture (CF); (**c**) semi-continuous fracture (SCF); (**d**) widened fracture (WF); (**e**) fresh granite.

4.3.3. Pore Network Distribution

The measured results of the physical properties of 58 granite samples show that the buried-hill reservoirs of the SNLU are highly heterogeneous (Figure 8). The distribution range of porosity is 0.05% to 19.45%, with an average of 6.28%. A porosity of more than 5% occurs most frequently, accounting for approximately 60%. The permeability distribution range is between 0.01 and 24.35 md, with an average of 4.11 md, and more than half of the permeability is below 1 md.

According to the buried depth of the granite, the reservoirs can be divided into three groups. In shallowly buried granite reservoirs (buried depth $\leq$ 1300 m), the physical properties are good, and the average porosity and permeability are 7.04% and 7.46 md, respectively. In moderately buried granite (buried depth between 1300 and 2000 m), the average porosity and permeability are 6.03% and 1.25 md, respectively. In deeply buried granite (buried depth $\geq$ 2000 m), the average porosity and permeability are 4.05% and 0.12 md, respectively. It is notable that permeability decreases rapidly with increasing buried depth, while porosity in deep granite is still considerable.
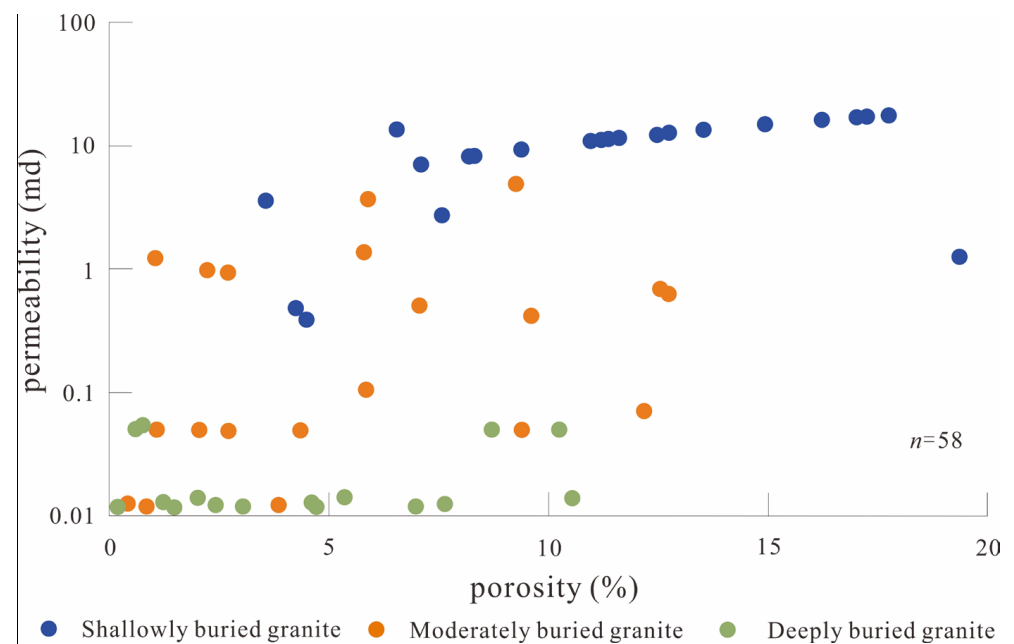
Figure 8. Cross-plot of porosity and permeability of granite from SNLU.

4.3.4. Seismic Reflection Characteristics

The seismic responses of granite buried hills are different from those of overlying sedimentary rocks, and there is a strong reflection interface between them. The seismic reflection of the weathering crust shows significant vertical zonation and varies with different structural positions in the profile. Strong amplitude and medium–weak continuity reflections dominate at the top of the structure. In the middle section of the weathering crust, granite is characterized by seismic reflections with medium–weak amplitude and weak continuity, changing to chaotic–blank reflections in the lower part. The net-like reflection is common in the study area, indicating that intersected fractures are well developed. Apparently, the closer the granite is to the top, the stronger the weathering intensity and reflection amplitude. The results of well seismic calibration show that the strong amplitude and medium–weak continuity reflections correspond to strongly weathered granite, the medium–weak amplitude and weak continuity reflections correspond to fractured granite, and the chaotic–blank reflections correspond to the bottom of weathering crust and fresh granite (Figure 9).
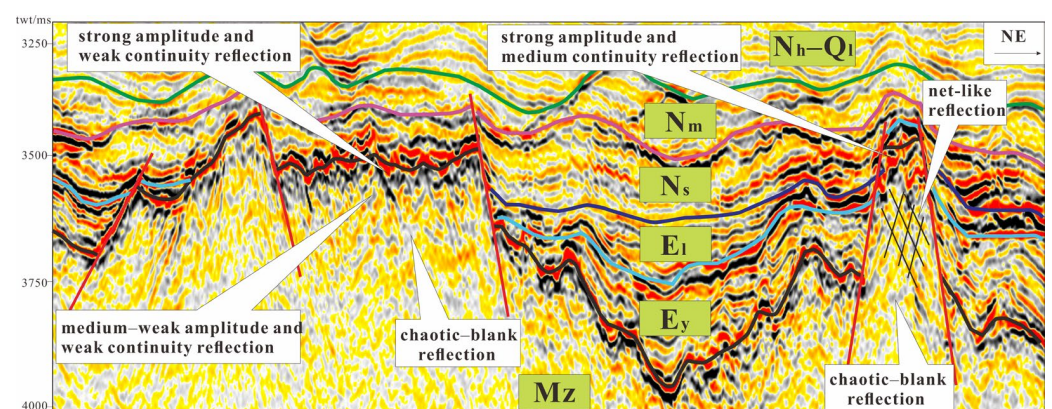

Figure 9. Seismic reflection characteristics of weathering crust in SNLU. The darker the color, the stronger the amplitude.

4.3.5. Outcrops

Through fieldwork, analogous Triassic granite outcrops were located in a quarry at Dawei Mountain in Liuyang, which help us better understand the structure of the weathering crust. With changes in elevation, the structure characteristics of weathering crust vary significantly (Figure 10a). Beneath the present land surface, massive weathered sandy conglomerates with clay are well preserved at the summit of Dawei Mountain, corresponding to the eluvial slope layer (Figure 10b). On the gentle slope nearby, the sandy granite is composed of loose weathered sandstone and clay. The calcite dyke without displacement implies that the granite is locally weathered (Figure 10c). Chemical weathering results in obvious dissolution in the weathered sandy layer, which is distinct from the overlying eluvial slope layer (Figure 10d). In the middle part of Dawei Mountain, the dissolution intensity decreases and fractures, especially high-angle fractures, are well developed. Some of them are blocked or partially blocked by weathering products, including clay minerals and small pieces of gravel. Fragmented regions can be observed (Figure 10e). The density of high-angle fractures decreases significantly at the foot of the mountain. This section is dominated by low-angle fractures and vugs, and the rock becomes denser with little weathered clay (Figure 10f).
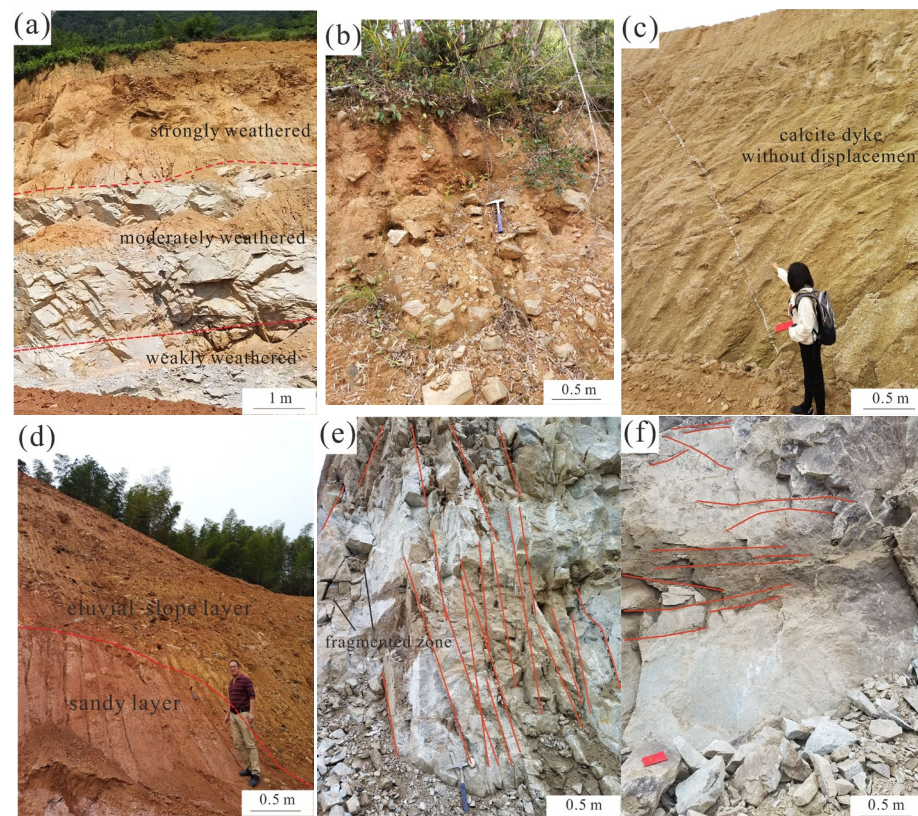
Figure 10. Granite outcrops of Dawei Mountain in Liuyang. (**a**) Whole structure of granite weathering crust with distinct zonation. (**b**) Well-preserved eluvial slope layer on top of Dawei Mountain, note massive gravels. (**c**) Weathered sandstone is loose and complete calcite dyke is visible. (**d**) Weathered sandy layer shows stronger dissolution compared to overlying eluvial slope layer. (**e**) Fragmented zone and perpendicular fractures (red line) in middle of Dawei Mountain. (**f**) Low-angle fractures (red line) and vugs at foot of Dawei Mountain.

5. Discussion

5.1. Vertical Zonation of Weathering Crust

Based on the characteristics of drill cores, FMI logs, thin sections, physical properties and outcrops, combined with seismic interpretation, the granite weathering crust of the

SNLU can be divided into the eluvium–slope zone (ESZ), sandy zone (SZ), weathered fracture zone (WFZ) and horizontal undercurrent vuggy zone (HUVZ), from top to bottom (Figure 11).

The ESZ mainly consists of a mixture of residual and short-transported gravel and/or massive granite, sandstone and clay. It is altered by mechanical reworking and rainwater erosion. Note that there is a very thin paleosol layer on top of the ESZ, but it is difficult to recognize. Therefore, this layer is considered to be part of the ESZ. Microfissures and intergranular dissolution pores are well developed in the ESZ. The porosity of this zone ranges from 0.18% to 10.55%, and the average is 4.68%. The permeability distribution range is between 0.06 and 13.2 md, with an average of 2.34 md. In the imaging log, the ESZ shows features of irregular bright masses on a dark background with dark clusters on the top. Seismic reflections of the ESZ show strong amplitude and weak continuity. The ESZ is only observed in well S832, and the thickness is 16.6 m.

zonation	structure	FMI	weathering intensity	core	storage space	seismic reflection characteristics
ESZ			strong		microfissures and intergranular dissolution pores	strong amplitude and weak continuity
SZ					intergranular and intragranular dissolution pores	strong amplitude and medium continuity
WFZ			moderate		structural and dissolution fractures	medium–weak amplitude and medium continuity
HUVZ			weak		vugs	chaotic–blank
Bedrock				Fresh granite		

Bedrock | HUVZ | WFZ | SZ | ESZ

Figure 11. Vertical zonation of granite weathering crust in SNLU. The FMI imaging log of the ESZ, SZ, WFZ, HUVZ and bedrock becomes brighter and brighter, showing that the weathering weakens gradually from (**top**) to (**bottom**). On top of the granite (ESZ + SZ), the cores are generally loose and mainly composed of residual sand and gravel. The core in the WFZ becomes denser and is filled with various high-angle fractures, while the rock in the HUVZ is slightly weathered to form low-angle fractures and vugs. As the weathering intensity gradually decreases, the seismic amplitude and continuity of the ESZ, SZ, WFZ and HUVZ appear to be weaker and weaker.

Due to the preservation of the overlying ESZ, the mechanical breakdown becomes weak and is replaced by strong chemical weathering. With meteoric water leaching, granite is thoroughly altered through hydration and hydrolysis, converting mineral particles such as feldspar, amphibole and biotite into clay. This layer is mainly filled with quartz grains and clay. The framework of the original rock is complete and loose like sandstone. Therefore, this layer is defined as the SZ. The main storage spaces of the SZ are intergranular and intragranular dissolution pores. The distribution range of porosity is between 2.69% and 19.76%, and the average porosity is 11.46%. The permeability is distributed between 0.05 and 13.9 md, with an average of 4.99 md. FMI logs show smaller bright spots with high resistivity in this zone than in the ESZ. The SZ is characterized by seismic reflections with

strong amplitude and medium continuity. The SZ, with an average thickness of 31.3 m, can be recognized in wells S811 and S832.

The ESZ and SZ are located on top of the granite structure, classified as a strongly weathered zone. They are the reservoirs with the best physical properties in the granite weathering crusts of the SNLU. During evolution, it was difficult to maintain the strong weathered zone due to subsequent denudation and water erosion.

As the depth increases, chemical weathering tends to become weaker, and the degree of consolidation of the granite becomes higher. The WFZ is composed of granite filled with numerous structural and diagenetic fractures. In this zone, meteoric water infiltrated along the existing fractures, dissolving and expanding the fracture system. In the highly fractured section, the granite is even broken into pieces, filled with smaller gravels and clay, and the WFZ consists mainly of a fragmentation layer or gravelly sandstone layer. The porosity of the WFZ is mainly in the range of 0.12% to 12.17%, with an average of 3.91%. The permeability distribution range is between 0.05 and 24.35 md, and the average permeability is 2.5 md. Continuous, incomplete and widened dark sinusoidal curves can be observed in the imaging logs. In the seismic profile, the WFZ shows reflection characteristics of medium to weak amplitude and weak continuity. These zones are distributed across all five exploration wells and have an average thickness of 113.6 m. As the thickest and the most stable reservoir in the weathering crust, the WFZ is a key hydrocarbon exploration target for the SNLU. The WFZ corresponds to a moderately weathered zone.

In general, a horizontal undercurrent zone often occurs in carbonate weathering crust [51–53]. In the case of granite, the rock can also be altered by groundwater in the same way, resulting in the development of a vuggy system with subhorizontal fractures. The HUVZ developed below the WFZ directly or interbedded with a bedrock layer, depending on the water table at that time. This zone could also have been reconstructed by subsequent uplift and subsidence. The reservoirs in the HUVZ are dominated by low-angle or/and horizontal dissolution fractures and vugs. The range of porosity distribution for this zone is between 0.45% and 4.75%, and the average is 2.7%. The permeability varies between 0.05 and 0.51 md, with an average of 0.23 md. In the imaging logs, the HUVZ is visualized as dark low-angle sinusoidal curves on a bright background, and bright-resistant masses represent vugs filled with calcite. In seismic profiles, chaotic–blank seismic reflections represent the HUVZ. This zone can be recognized in wells S831, S832, S811 and S811, with an average thickness of 56.3 m. The HUVZ belongs to a weakly weathered zone.

5.2. Genetic Mechanism of Weathering Crust Reservoirs

5.2.1. Petrology and Minerals

Due to the different weathering resistance of minerals, mineral composition is vital to the development of secondary pores and fractures in the weathering crust [6,54,55]. Bright minerals, such as feldspar and quartz, are brittle and can be easily affected by tectonic stresses, which makes the granite become integrated and form structural fractures [56]. In addition, feldspar has weak anti-weathering ability and can form dissolution pores and widened fractures through water–rock reactions [57]. Dark minerals such as amphibole and biotite are relatively hard and do not break easily to form cracks. The darker the minerals, the fewer the storage spaces [58].

The mineralogical results show that the main petrology of the SNLU basement is monzonitic granite and granodiorite (Figure 3), and the content of felsic minerals is greater than 80% (Table 2). The rich felsic minerals of the granite provide the basis for fracture formation and fluid dissolution. The granite structure in the study area underwent multistage tectonism and long-term weathering throughout geological history. Complex stresses led to the mechanical fragmentation of brittle minerals and thus the formation of numerous structural fractures. Through the leaching of meteoric water and acidic fluid along fractures, felsic minerals, particularly feldspar, were hydrated, hydrolyzed and acidified, resulting in the formation of various dissolution pores and widened fractures.

A comparison of distinct weathering crust structures in wells S811 and S832 shows that the thickness and reservoir properties of the weathering crust are greater in monzonitic granite than in granodiorite (Table 4). Obviously, the higher content of biotite makes the granodiorite tougher and more plastic and makes it more difficult to form fractures and undergo dissolution. That is, fewer physical breakdowns occur in granodiorite, resulting in a thinner WFZ and poor permeability; less chemical weathering occurs in the mafic minerals, leading to a thinner strongly weathered zone and poor reservoir properties of granodiorite.

Table 4. Comparison of weathering crust in wells S811 and S832.

Well	Petrology	Thickness/m		Porosity (Avg.)/%	Permeability (Avg.)/md
		ESZ + SZ	WFZ		
S811	Monzonitic granite	62	135	0.76–19.76 (7.69)	0.05–24.35 (4.76)
S832	Granodiorite	45	126	0.18–15.07 (4.64)	0.05–17.24 (3.42)

5.2.2. Long-Term Weathering and Warm–Humid Paleoclimate

The formation of granite weathering crust takes thousands of years, and there is a positive non-linear exponential relationship between weathering thickness and time [59,60]. In addition, the exposed environment plays an indispensable role in the formation of weathered granite reservoirs. The thickness and physical properties are better for weathering crust developing under warm and wet conditions than under cold and dry conditions. When the climate is cold and dry, granite suffers mainly mechanical deformations with few chemical and biological alterations, resulting in a lack of dissolution pores and fractures [25,61,62].

The results of zircon U–Pb dating indicate that the SNLU granite was crystallized in the Early to Middle Triassic. After being exposed in the Late Cretaceous, the granite was completely buried until the Miocene [32]. That is, it has been weathered and eroded for 42 million years or even longer, which is enough to form large-scale economic reservoirs. Pollen data show that the Oligocene pollen assemblages of S812 in the study area are dominated by *Polypodiisporites*, *Polypodiaceaesporites haardti* and *Triletes* of the tropical–subtropical Pteridophyta, *Pinuspollenites* of the temperate alpine Gymnospermae and *Quercoidites* of the evergreen Angiosperms (Figure 12). The Yacheng formation pollen assemblages of S131 also contain high contents of *Polypodiaceaesporites haardti*, *Triletes*, *Polypodiisporites* and *Pinuspollenites*. These results reveal that the environment in the study area was warm and humid during the Oligocene [63,64], contributing to various types of chemical and biological weathering.

5.2.3. Faults

For dense granite geological bodies, weathering and leaching during the exposure period only change the upper part of the granite structure and have little effect on the deeper part. As major reservoir spaces in weathering crust reservoirs, fractures are mainly controlled by faults. Many studies suggest that the fracture density of granite is negatively correlated with the distance to the deep fault. The closer it is to fault belts, the more fractures there are [5,65].

The variance cube slice of the study area shows that there are mainly two groups of faults in the SNLU that developed under the influence of complex stress fields: NW–SE and NE–SW trending faults (Figure 13a). These faults disintegrated the granite and created channels for atmospheric water leaching, forming dissolution pores and fractures on top of the granite structure and accelerating the weathering process in the deeper parts. In addition, large-scale faults are always accompanied by a large number of fractures. Both of them constitute a widely spreading meteoric water translocation system, expanding

weathering interfaces and facilitating the formation of thick weathering crust near faults. The NW–SE and NE–SW trending fractures can be recognized from the image logs of the SNLU (Figure 13b). The dips of the NW–SE trending fractures range from 28.3° to 73.4°, and medium-angle fractures (30°–60°) occur with the highest frequency (about 60% of the total). The maximum dip of the NE–SW trending fractures is 72.5°, and the minimum dip is 18.9°. High-angle fractures (60°–90°) and medium-angle fractures account for the largest proportion (74.8% of the total). The fractures are not only effective storage spaces for weathering crust but also significantly improve the connectivity of reservoirs. Apparently, fault-related fractures favor the development of weathering crust reservoirs in the SNLU.
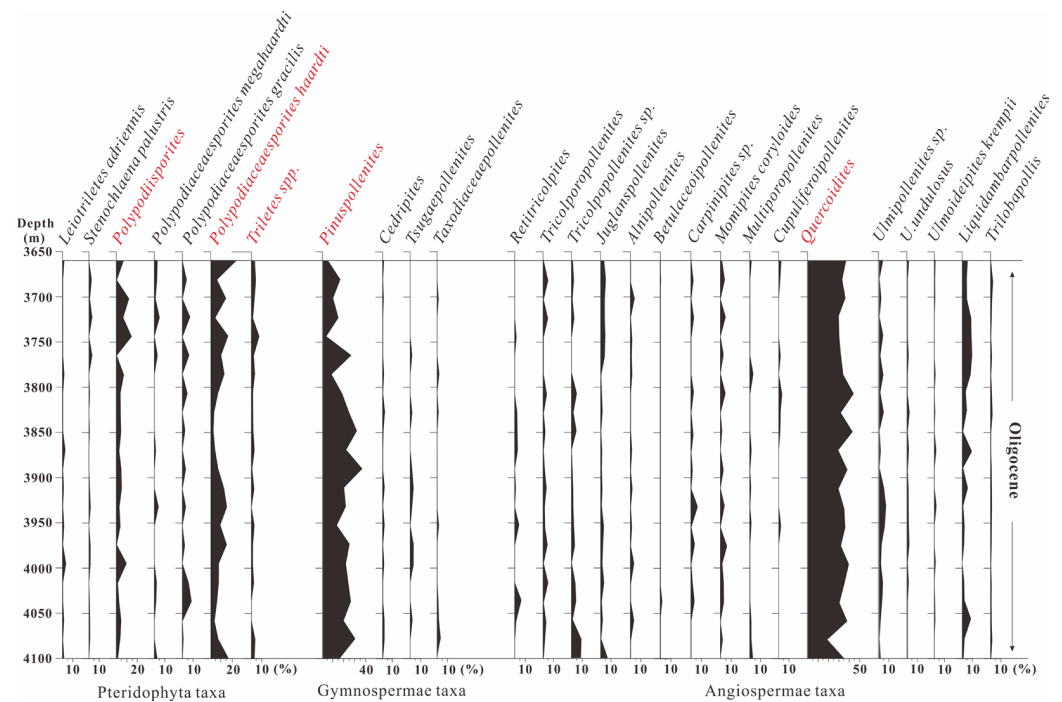
Figure 12. Oligocene palynological assemblages in SNLU.
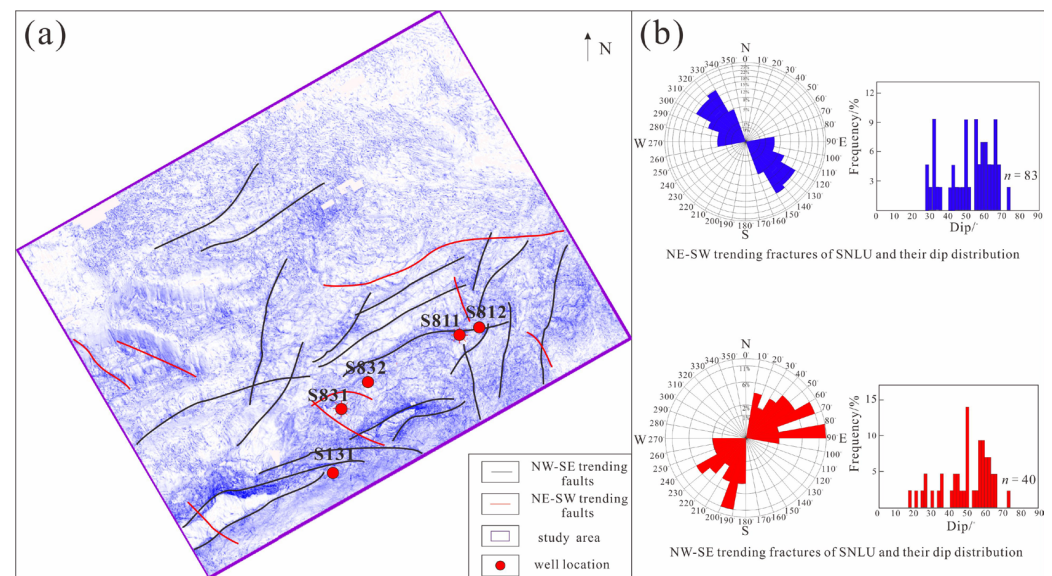
Figure 13. Fracture characteristics of SNLU: (**a**) variation cube slice of study area; (**b**) distribution of trends and dips of conductive fractures in SNLU.

5.2.4. Topography

Studies on weathering crusts of the Penglai 9-1 oil and gas fields in the Bohai Bay Basin and the Dongping district in the Qaidam Basin indicate that a gentle slope of the structure provides a favorable location for the development and maintenance of high-quality reservoirs [10,15,16], and the structure of weathering crust varies with different topographies [25,65,66].

In the study area, the vertical structures of the weathering crust in five exploration wells are not identical. WFZ and HUVZ can be observed in wells S131, S831, S812, S811 and S832, while ESZ and SZ are developed only in the latter two. In the cross-well geological profile, well S832 is located in a flat landform at high elevation. The weathering crust in this topography is not easily influenced by geological agents such as water and gravity. The paleosol is easily preserved, with lush vegetation, and provides protection for residual weathered clastic grains. Wells S831 and S131 are located on steep slopes of the structure, and unstable ESZ and SZ in the top section are missing due to strong fluid flushing and sparse vegetation. Well S811 is located in the graben-type structural highland with a gentle slope, where the ESZ is washed away and the SZ remains. Well S812 is located in the valley, a deeper structural position, where the ESZ and SZ are hardly preserved due to water erosion (Figure 14). That is, different topographies have led to the differential development of weathering crust structures in the study area.

In addition, although the paleogeomorphological highs were in a strong denudation zone, they may have developed thicker weathering crust reservoirs due to longer weathering, especially the strongly and moderately weathered zones. More specifically, the weathering crust in wells S831, S832 and S811, covered by the Neogene sediments, is thicker than that in wells S131 and S812, covered by the Paleogene depositions. Obviously, weathering crusts that developed in higher topographies show a better quality of reservoir than those in the lower parts of the SNLU.
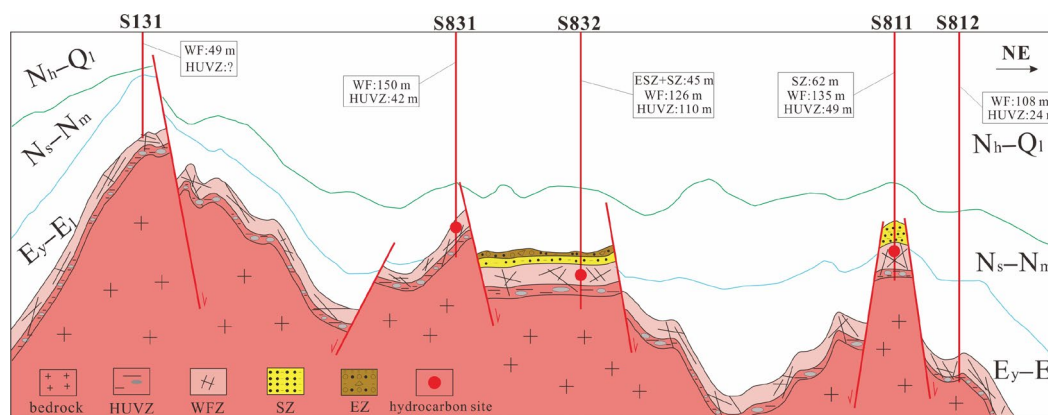

Figure 14. Geological cross-well profile of study area (profile location seen in Figure 1). The symbol "?" implies the HUVZ is not undrilled in Well S131.

5.2.5. Shallow Buried Depth

For sedimentary rocks, buried depth has a significant influence on porosity and permeability. Many studies show that the physical properties of granite reservoirs appear to be influenced by the buried depth [5,52,67].

The relationship between porosity and buried depth shows that the porosity of clastic rocks in the deep-water area of the QDNB decreases with buried depth (Figure 15a). The porosity of the strongly weathered zone also has a negative correlation with buried depth due to the similar structure of clastic rocks. With increasing depth, diagenesis is gradually enhanced. Under deep burial, intergranular pores and fractures of the strongly weathered zone can be cemented by weathered clay or even disappear. Studies on granite reservoirs of the Bach Ho and La Paz fields indicate that buried depth over 3500 m leads to destructive

diagenesis on the weathered rind [5,23]. The buried depth of strongly weathered reservoirs in the study is 1000–1500 m, and destructive diagenesis is weak in this interval filled with weathered gravels, sandstone and clay. Side-wall core and thin sections of the SZ show that the lithology is loose, and the reservoir spaces are characterized by disintegrated low-contact quartz and feldspar particles, suggesting weak compaction (Figure 15b,c). That is, small alterations caused by diagenesis occur in the strongly weathered zone due to the shallow buried depth, leading to the formation of high-quality weathering crust reservoirs in the study area.
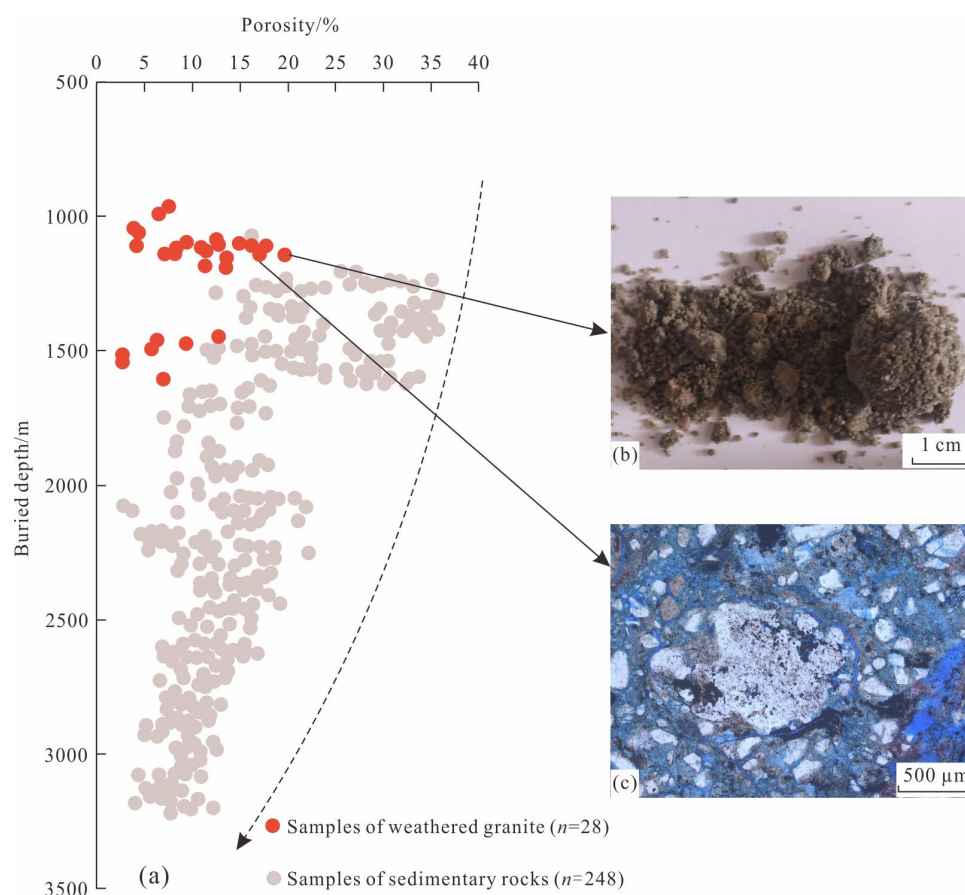
Figure 15. Relationship between physical properties and buried depth in deep-water area of QDNB: (**a**) porosity decreases with increasing buried depth; (**b**) loose side-wall core of SZ; (**c**) thin section of SZ showing well-developed intergranular dissolution pores.

5.3. Development Pattern of Weathering Crust

A development model of the weathering crust in the SNLU was determined based on the vertical division and genetic mechanism (Figure 16).

On the top of the granite buried hill, long-term weathering and leaching create a strongly weathered zone. In the flat terrain, the ESZ is well preserved, and the vertical structure of the weathering crust is complete. However, weathered granite, composed of mud-bearing sandy conglomerates, is absent on the bump-shaped top of the granite, where it is easily washed away and accumulates in the lower gentle slope. According to outcrop observations and an analysis of the cross-well profile, loose strongly weathered reservoirs are also easily eroded by geological agents in the steep slope of the structure. The middle part of the structure mainly corresponds to the WFZ. It is difficult for this zone to be affected by water erosion and diagenesis due to its granite structure. The penetration and dissolution of meteoric water greatly enlarge and widen the fracture system, making the WFZ the most wide-spread and thickest granite reservoir. The WFZ at the foot of the

slope is covered by what is probably sedimentation of alluvial delta or fan delta derived from the denudation of weathering crust at higher elevations. Below, the HUVZ is mainly influenced by the groundwater and distributed along the WFZ. Although the cross-well profile shows that the HUVZ is widely developed and reconstructed by tectonism, it cannot be an exploration target due to poor connectivity between vugs.
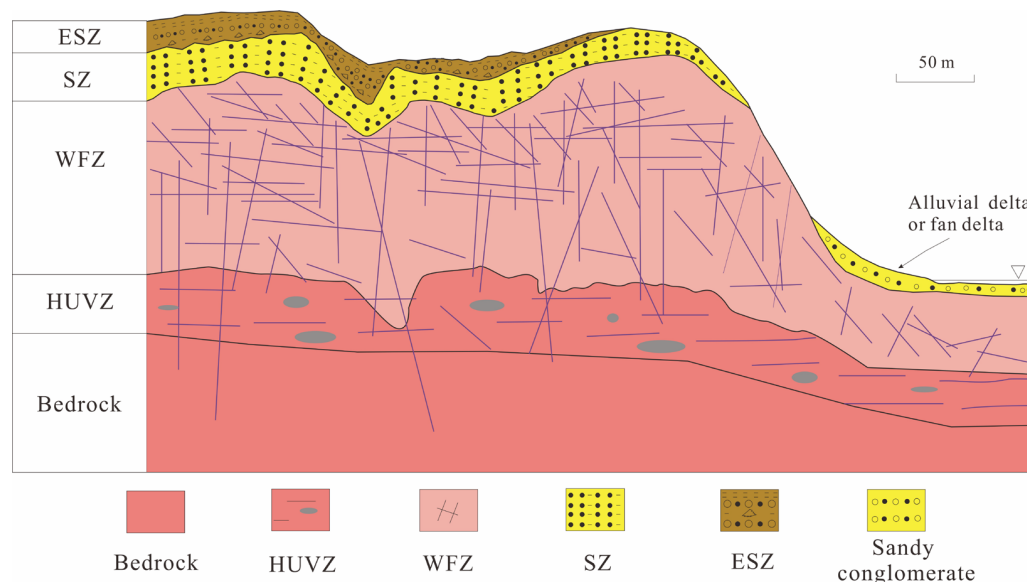
Figure 16. Development pattern of weathering crust reservoirs in SNLU. From top to bottom, reservoir type and weathering product vary with the decreasing weathering intensity. Horizontally, the structures of weathering crust vary with different topographies. The triangle symbol implies the sea level.

5.4. Evolution Process of Granite Weathering Crust

With the continuous discovery of granite reservoirs around the world, many scientists have established different development models of weathering crust based on the existing structure, but few mention the multistage evolution of granite reservoirs [7,11,20,22,25,58,68]. Like any ordinary geological body, the weathering crust has been constantly altered by weathering and tectonism. Therefore, the use of a dynamic viewpoint is proposed to characterize the complex evolution process of granite reservoirs.

In recent years, scientists have reconstructed the geothermal history of granite in the Penglai oilfield and the Pearl River Basin based on constraints from ATF [69–71]. The results show that the estimated erosion thickness of the granite is over 2000 m. That is, the weathering crust reservoirs have suffered significant destruction/denudation [40,72–74]. To better understand the multistage development of granite reservoirs, an evolutionary model in conjunction with the thermal history of the SNLU is established in this paper.

The AFT inverse models of multiple samples in the study area are presented in Figure 17. They show overall similar thermal histories, as the SNLU has a very complex thermal history, undergoing five distinct stages since the formation of the granite: (1) post-magmatic rapid uplifting during about 100–88 Ma at a cooling rate of ~4.1 °C/Ma, (2) slow cooling during about 88–45 Ma at a rate of ~1.1 °C/Ma, (3) accelerated uplifting during about 45–23 Ma with a cooling rate of ~3.1 °C/Ma, (4) slow subsiding during about 23–8 Ma at a heating rate of ~1.3 °C/Ma and (5) accelerated heating from about 8 Ma to the present at a rate of ~3.0 °C/Ma.
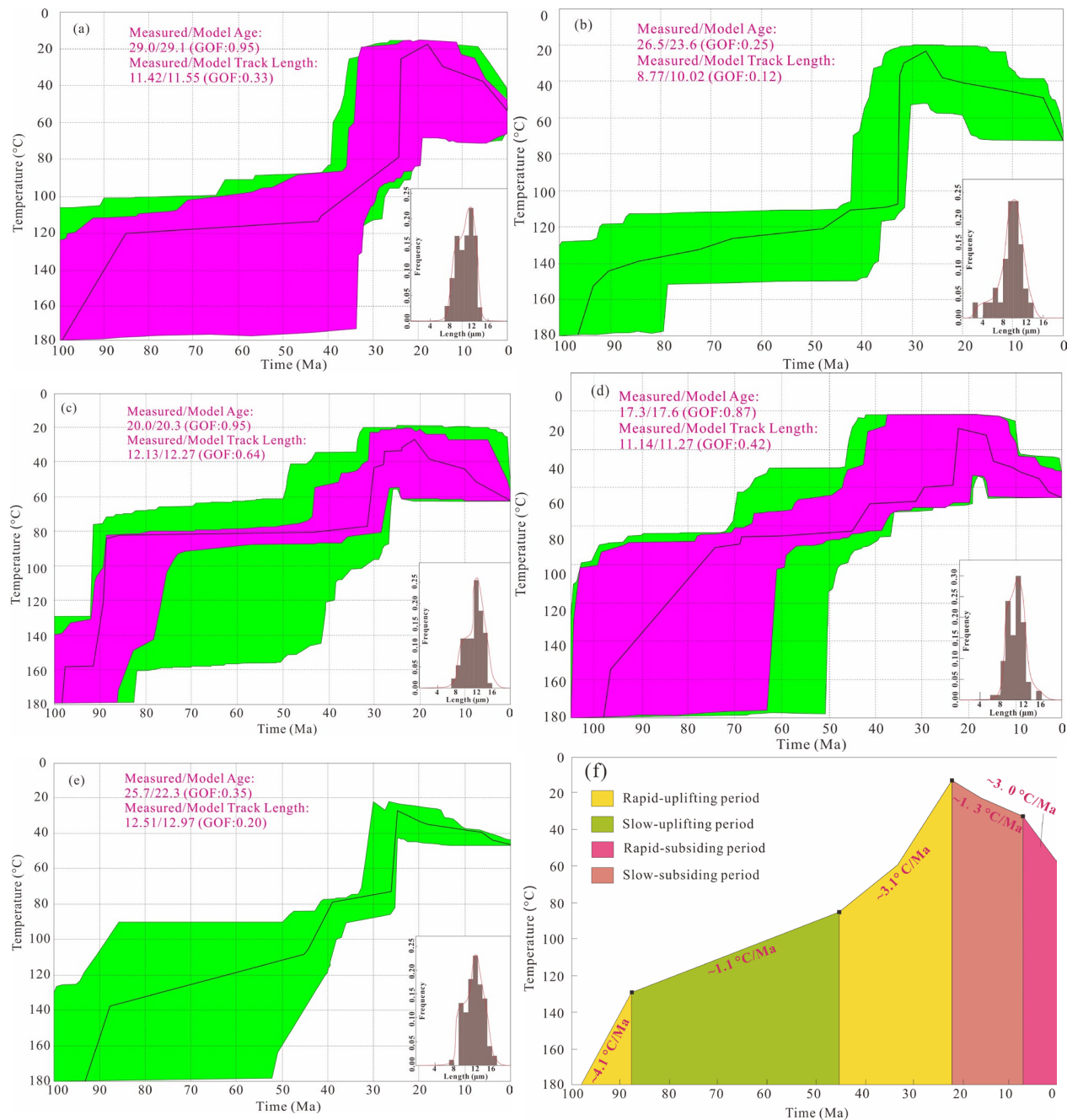
**Figure 17.** Thermal history of wells in SNLU: (**a**) well S811; (**b**) well S812; (**c**) well S831; (**d**) well S832; (**e**) well S131. (**f**) Comprehensive thermal history of SNLU granite structure. Green envelope is covered by "acceptable fit" temperature–time paths, rose envelope is covered by "good fit" temperature–time paths, and solid black lines represent best-fit temperature–time paths. GOF, goodness of fit.

Based on the thermal modeling results, the uplift–subsidence pattern of the granite structure in the SNLU is reconstructed (Figure 18). In stage I, the magma intruded into the surrounding rock as part of the collision and extrusion of the Pacific Plate and the India Plate in the Early Triassic [75]. In stage II, after the accelerated uplift during the Late Cretaceous, the Mesozoic granite was exposed in the Paleocene Lile movement [73]. Under the influence of tectonism and paleo-karstification, the WFZ and HUVZ initially emerged. After long-term mechanical reworking and chemical weathering, the upper part of the WFZ gradually transformed into ESZ and SZ, and the complete structure of the

original weathering crust was formed. In stage III, with continuous rapid exhumation in the Eocene Xiwei movement, the strongly weathered zone on top of the granite was destructed and denuded, with only the WFZ remaining. In stage IV, the upper part of the WFZ was again altered and corroded by long-term weathering and leaching; the strongly weathered zone was regenerated in the Oligocene. In stage V, the basement began to subside slowly until the Miocene, and sediments subsequently covered the entire study area. As a result, the weathering crust was preserved with a complete structure. That is, the weathering crust reservoirs had undergone an evolutionary process of formation–destruction/denudation–regeneration–preservation. The weathering crust, especially the strongly weathered zone, could not be preserved with continuous uplifting. It was easily destroyed and eroded by various weathering processes. Note that there may have been several cycles for the destruction/denudation–regeneration process throughout geological history. The evolutionary process would proceed to the "preservation" stage only when the granite massif stopped rising, became stable and was buried by sediments. Then, the recycling process ended, and the structure of the present weathering crust reservoir was accomplished.
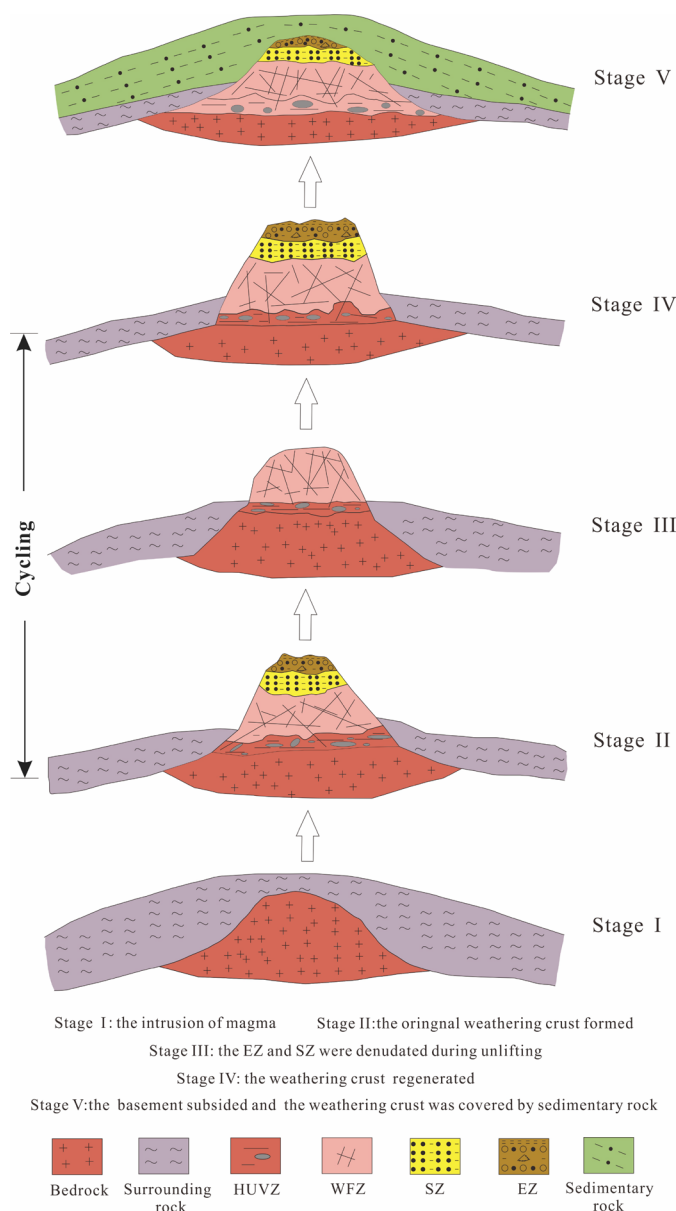

Figure 18. Evolution process of weathering crust reservoir.

5.5. Prediction of Favorable Reservoirs

Based on the development pattern of weathering crust reservoirs and hydrocarbon testing data, the distribution of favorable reservoirs in the SNLU is predicted following the principle of differential accumulation of hydrocarbons. The results show that the top sections of the structure, with a platform or gentle slope, are the favorable locations. Known from the genetic mechanism of granite reservoirs mentioned above, these topographies help to preserve the ESZ and SZ with excellent physical properties. The thickness of mature marine source rock from the Yacheng formation in the adjacent Songnan-Baodao Sag can reach up to 3000 m. Hydrocarbons migrated along the structure ridge to the study area and accumulated in the highlands. Moreover, fractures also provided conduits for the lateral migration of oil and gas. In addition, the thick Oligocene and Miocene mudstone provided shelter for weathering crust reservoirs, effectively inhibiting oil and gas from escaping. These factors greatly increase the probability of granite reservoirs at site A and B bearing oil and gas. According to oil and gas testing data from the Zhanjiang branch of the CNOOC, the proven thickness of the gas reservoir in S832 is more than 80 m, which indicates high credibility of hydrocarbon-bearing zones in the predicted reservoirs (Figure 19).
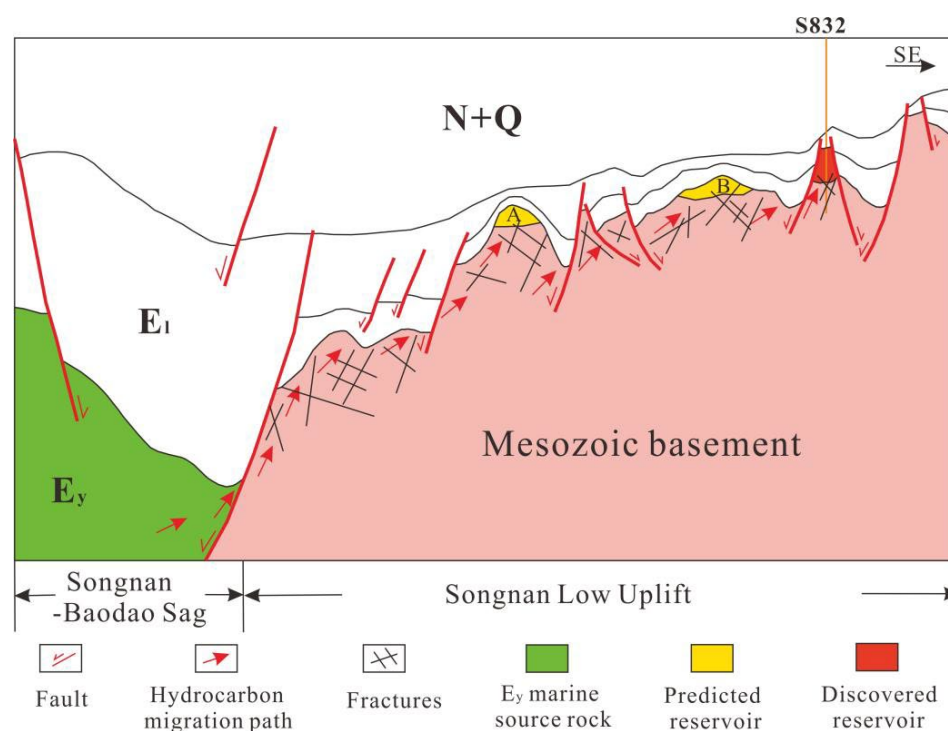
Figure 19. Prediction of favorable reservoirs in study area.

6. Conclusions

(1) The weathering crust of the Songnan Low Uplift can be divided into eluvium–slope and sandy zone (strongly weathered zone), weathered fracture zone (moderately weathered zone) and horizontal undercurrent vuggy zone (weakly weathered zone), from top to bottom. The eluvium–slope zone mainly has microfissures and intergranular dissolution pores with an average porosity of 4.68% and permeability of 2.34 md. The sandy zone primarily consists of intragranular and intergranular dissolution pores with an average porosity of 11.46% and permeability of 4.99 md. The reservoirs, with excellent physical properties in the strongly weathered zone, are distributed on the top of the weathering crust. The weathered fracture zone is dominated by various fractures and dissolution pores along fractures, with an average porosity of 3.91% and permeability of 2.5 md; these are the thickest and most stable reservoirs in the middle of the weathering crust. The horizontal undercurrent vuggy zone,

at the bottom of the weathering crust, is mostly composed of low-angle fractures and vugs, with an average porosity of 2.7% and permeability of 0.23 m and poor hydrocarbon-bearing properties.

(2) The formation of granite reservoirs in the Songnan Low Uplift was controlled by various factors. The felsic minerals, making up more than 80%, comprise the material foundation for the development of fractures and dissolved pores. Long-term exposure and a warm, wet environment contributed to constant weathering and leaching. Multistage tectonic movements were beneficial for fracture development. Various topographies resulted in different structures of weathering crust. Shallow buried depth and weak diagenesis are beneficial for protecting reservoir spaces.

(3) Strongly weathered zones, including the ESZ and SZ, are mainly distributed in topographies with a gentle slope and platform on the top of the structure. The WFZ, a moderately weathered zone, is widely developed in the granite buried hills and covered by what may be sedimentation of alluvial delta or fan delta. At the bottom of the weathering crust, the weakly weathered HUVZ has been reformed by faults and is distributed along groundwater.

(4) The granite in the SNLU underwent long-term exhumation from the Late Cretaceous to the Miocene. The present weathering crust is the product of granite undergoing a complicated evolutionary process of formation–destruction/denudation–regeneration–preservation.

References

1. Jiao, X.; Niu, H.; Xie, Q.; Zattin, M.; Zhang, Y.; Wu, Z.; Chen, Y.; Zhao, X.; Liu, S.; Wei, X. Insights into the Weathering Crust Reservoirs of Granitoids: A Case Study from Qinghai Oilfield of Qaidam Basin, Northwest China. *Minerals* **2023**, *13*, 23. [CrossRef]
2. Zhang, Y.Y.; Wu, T.; Gou, W. Reservoir characteristics and hydrocarbon accumulation models of the Bach Ho oilfield in Cuu Long Basin, Vietnam. *Geol. Explor.* **2023**, *59*, 170–187.
3. Ye, T.; Chen, A.Q.; Yang, H.F.; Huang, Z.; Luo, J. Tectonism and fracture-related dissolution induced the formation of the large-scale metamorphic granite reservoir: Implications from Bozhong 26-6 Precambrian bedrock trap, offshore Bohai Bay basin, Northern China. *Mar. Pet. Geol.* **2023**, *160*, 106593. [CrossRef]
4. Pan, J.G.; Hao, F.; Zhang, H.Q.; Wei, P.S.; Zhang, J.L. Formation of granitic and volcanic rock reservoirs and their exploration potential. *Nat. Gas Geosci.* **2007**, *18*, 380–385.
5. Cuong, T.X.; Warren, J.K. Bach Ho Field, A Fractured Granitic Basement Reservoir, Cuu Long Basin, Offshore SE Vietnam: A "Buried-Hill" Play. *J. Pet. Geol.* **2009**, *32*, 129–156. [CrossRef]
6. Gong, Z.S. Continued exploration of granitic reservoir hydrocarbon accumulation in China offshore basin. *China Offshore Oil and Gas* **2010**, *22*, 214–220.
7. Dou, L.R.; Wei, X.D.; Wang, J.C.; Li, J.L.; Wang, R.C.; Zhang, S.H. Characteristics of granitic basement rock buried-hill reservoir in Bongor Basin, Chad. *Acta Pet. Sin.* **2015**, *36*, 897–904.
8. Wang, X. *The Hydrocarbon Accumulation Conditions and Accumulation Model of Granite Buried Hill in Penglai9-1 Structure*; Chengdu University of Technology: Chengdu, China, 2015; pp. 7–16.
9. Wang, X.; Zhou, X.H.; Xu, G.S.; Liu, P.B.; Gao, S.S.; Guan, D.Y. Characteristics and controlling factors of reservoirs in Penglai9-1 large-scale oilfield in buried granite hills, Bohai Sea. *OilGas Geol.* **2015**, *36*, 262–270.
10. Zhu, M.L.; Liu, Z.; Liu, H.M.; Li, X.K.; Liang, S.Z.; Gong, J.Q.; Zhang, P.F. Structural division of granite weathering crusts and effective reservoir evaluation in the western segment of the northern belt of Dongying Sag, Bohai Bay Basin, NE China. *Mar. Pet. Geol.* **2020**, *121*, 104612. [CrossRef]

11. Deng, Y.H.; Peng, W.X. Discovering large buried-hill oil and gas fields of migmatitic granite on Jinzhou 25-1S in Bohai sea. *China Offshore Oil Gas* **2009**, *21*, 145–150.

12. Ruxton, B.P.; Berry, L. Weathering of granite and associated erosional features in Hong Kong. *Bull. Geol. Soc. Am.* **1957**, *68*, 1283–1292. [CrossRef]

13. Price, D.G. A suggested method for the classification of rock mass weathering by a rating system. *Q. J. Eng. Geol.* **1993**, *26*, 69–76. [CrossRef]

14. Dewande, B.; Lachassagne, P.; Wyns, R. A generalized 3-D geological geological and hydrogeological conceptual model of granite aquifers controlled by single or multistage weathering. *J. Hydrol.* **2006**, *330*, 260–284. [CrossRef]

15. Wang, M.C.; Guan, D.Y.; Liu, P.B.; Zhang, C.; Su, K.; Ren, J. Characteristics and Formation Conditions of the Penglai 9-1 Granite Oil Reservoir in Bohai Gulf Basin. *Geol. Sci. Technol. Inf.* **2016**, *35*, 83–88.

16. Hu, Z.W.; Xu, C.G.; Yang, B.; Huang, Z.; Su, W. Reservoir forming mechanism of Penglai9-1 granite buried-hills and its oil geology significance in Bohai Sea. *Acta Pet. Sin.* **2017**, *38*, 274–285.

17. Wang, J.C.; Dou, L.R.; Xu, J.G.; Wei, X.D.; Wang, X.F.; Chen, H.Z. Application of "two wide and one high" seismic data in the characterization of granite buried-hill reservoirs: A case study of the Bongor Basin. *Pet. Geophys. Explor.* **2018**, *53*, 320–328.

18. Xu, S.L.; You, L.; Mao, X.L.; Zhong, J.; Wu, S.J. Reservoir Characteristics and Controlling Factors of Granite Buried Hill in Songnan Low Uplift, Qiongdongnan Basin. *Earth Sci.* **2019**, *44*, 2717–2728.

19. Hu, J.S.; Jiang, Y.M.; Tang, H.F.; Ma, W.R.; Tao, P.; Sun, N.Y. Quantitative characterization of vertical zonation of Mesozoic granite weathering reservoirs in the coastal area of eastern Fujian Province, China. *Pet. Sci.* **2023**, *2023*, 2664–2682. [CrossRef]

20. Li, J.P.; Zhou, X.H.; Wang, Q.B. Control of epigenic karstification over weathering crust reservoir development of Penglai granite buried hill oilfield, Bohai Bay Basin, China. *Chengdu Univ. Technol.* **2014**, *41*, 556–566.

21. Zhou, J.; Yang, X.B.; Yang, J.H.; Wu, H.; He, X.H.; Song, A.X. Development characteristics and formation mechanism of Mesozoic buried hill fractures in the deep water area of Qiongdongnan basin: Taking Y8 area in Songnan low uplift as an example. *China Offshore Oil Gas* **2020**, *32*, 1–9.

22. Ye, T.; Niu, C.M.; Wei, A.J. Characteristics and genetic mechanism of large granitic buried-hill reservoir, a case study from PengLai oil field of Bohai Bay Basin, north China. *J. Pet. Sci. Eng.* **2020**, *189*, 106988. [CrossRef]

23. Nelson, R.A.; Moldovanyi, E.P.; Matcek, C.C.; Azpiritxaga, I.; Bueno, E. Production characteristics of the fractured reservoirs of the La Paz Field, Maracaibo basin, Venezuela. *AAPG Bull.* **2000**, *84*, 1791–1809.

24. Ye, T.; Sun, S.; Chen, A.Q.; Niu, C.M.; Luo, J.; Hou, M.C. The formation and architecture of Penglai granite intrusion reservoir along theTanlu strike-slip fault: Implications for basement exploration in the offshore Bohai Bay Basin, North China. *Energy Rep.* **2023**, *9*, 1291–1307. [CrossRef]

25. Huang, J.H.; Tan, X.F.; Cheng, C.J.; Li, Z.M.; Ma, L.J.; Zhang, H.L.; Wu, Y.X. Structural features of weathering crust of granitic basement rock and its petroleum geological significance: A case study of basement weathering crust of Dongping area in Qaidam Basin. *Earth Sci.* **2016**, *41*, 2041–2060.

26. Wei, X.S.; Ren, J.F.; Zhao, J.X.; Zhang, D.F.; Luo, S.S.; Wei, L.B.; Chen, J.P. Paleogeomorphy evolution of the Ordovician weathering crust and its implication for reservoir development, eastern Ordos Basin. *Pet. Res.* **2018**, *3*, 77–89. [CrossRef]

27. Wu, S.G.; Yuan, S.Q.; Zhang, G.C.; Ma, Y.B.; Mi, L.J.; Xu, N. Seismic characteristics of a reef carbonate reservoir and implications for hydrocarbon exploration in deepwater of Qiongdongnan Basin, northern South China Sea. *Mar. Pet. Geol.* **2009**, *26*, 817–823. [CrossRef]

28. Sun, Q.L.; Wu, S.G.; Lu, F.L.; Yuan, S.Q. Polygonal faults and their implications for hydrocarbon reservoirs in the southern Qiongdongnan Basin, South China Sea. *J. Asian Earth Sci.* **2010**, *39*, 470–479. [CrossRef]

29. Wang, Z.F.; Li, X.S.; Sun, Z.P.; Huang, B.J.; Zhu, J.T.; Yao, Z.; Guo, M.G. Hydrocarbon accumulation conditions and exploration potential in the deep-water region, Qiongdongnan Basin. *China Offshore Oil Gas* **2011**, *23*, 7–13.

30. Huang, B.J.; Tian, H.; Li, X.S.; Wang, Z.F.; Xiao, X.M. Geochemistry, origin and accumulation of natural gases in the deepwater area of the Qiongdongnan Basin, South China Sea. *Mar. Pet. Geol.* **2016**, *72*, 254–267. [CrossRef]

31. Feng, Y.W.; Qu, H.J.; Zhang, G.C.; Pu, R.H. Seismic interpretation and hydrocarbon accumulations implication of the Miocene Meishan Formation reefs in southern Qiongdongnan Basin, northern South China Sea. *J. Palaeogeogr.* **2017**, *6*, 206–218. [CrossRef]

32. Yang, J.H.; Huang, B.J.; Yang, J.H. Gas accumulation conditions and exploration potentials of natural gases in Songnan low uplift, deep water area of Qiongdongnan Basin. *China Offshore Oil Gas* **2019**, *31*, 1–10.

33. Guo, M.G.; Zeng, X.Y.; Jiang, R.F.; Zhu, J.T.; Sun, Z.P.; Mao, X.L.; Man, X.; He, X.H. The formation condition of multiple oil and gas accumulation and accumulation model of Songnan low uplift in deep-water area of Qiongdongnan Basin. *Contrib. Geol. Miner. Resour. Res.* **2017**, *32*, 577–587.

34. Tang, L.S.; Zhu, J.T.; Yao, Z.; Guo, M.G.; Mao, X.L. Evolution and reservoir formation conditions of buried hills in Songnan Low Uplift of the Qiongdongnan Basin. *Spec. Oil Gas Reserv.* **2017**, *24*, 87–91.

35. Sun, W.Y.; Deng, Y.; Hu, L.; Liu, S.Y.; Liao, J.; Wang, R. Study and application of geophysical characteristics and evaluation technique of basement buried-hill of Songnan low uplift in the deep water area of Qiongdongnan Basin. *Comput. Tech. Geophys. Geochem. Explor.* **2021**, *43*, 323–330.

36. Song, A.X.; Yang, J.H.; Yang, J.H.; Hu, B.; Wang, L.J.; Lu, X. Zoning characteristics of buried hill reservoir and prediction of favorable reservoir in the western deep water area of South China Sea. *China Offshore Oil Gas* **2020**, *32*, 54–63.

37. Yang, X.B.; Zhou, J.; Yang, J.H.; He, X.H.; Wu, H.; Gan, J.; You, J.J. Natrual gas source and accumulation model of Mesozoic buried hill in the eastern deep water area of Qiongdongnan Basin. *Acta Pet. Sin.* **2021**, *42*, 283–292.

38. Hu, B.; Wang, L.S.; Yan, W.B.; Liu, S.W.; Cai, D.S.; Zhang, G.C.; Zhong, K.; Pei, J.X.; Sun, B. The tectonic evolution of the Qiongdongnan Basin in the northern margin of the South China Sea. *J. Asian Earth Sci.* **2013**, *77*, 163–182. [CrossRef]

39. Zhang, G.C.; Mi, L.J.; Wu, J.F.; Shen, H.L.; Yang, D.S.; Song, S. Rises and their plunges: Favorable exploration directions for major in the deepwater area, Qiongdongnan Basin. *China Offshore Oil Gas* **2010**, *22*, 360–368.

40. Zhou, J.; Yang, X.B.; Yang, J.H.; Gan, J.; Wu, H.; He, X.H.; Hu, B. Structure-Sedimentary Evolution and Gas Accumulation of Paleogene in Songnan Low Uplift of the Qiongdongnan Basin. *Earth Sci.* **2019**, *44*, 2704–2716.

41. Gan, J.; Zhang, Y.Z.; Liang, G.; Yang, X.B.; Li, X.; Song, P. Deposition Pattern and Differential Thermal Evolution of Source Rocks, Deep Water Area of Qiongdongnan Basin. *Earth Sci.* **2019**, *92*, 2359–2367.

42. Sun, R.; Han, Y.X.; Zeng, Q.B.; Wang, X.Y.; Zhang, G.C.; Zhao, Z.G.; Yang, H.C.; Yao, X.Z. Sedimentary characteristics of Yacheng Formation in the eastern deepwater in Qiongdongnan Basin and their control on marine source rocks. *Acta Pet. Sin.* **2019**, *40*, 57–66.

43. Huang, B.J.; Li, X.S.; Wang, Z.F.; Li, L.; Huang, Y.W. Source rock geochemistry and gas potential in the deep water area, Qiongdongnan Basin. *China Offshore Oil Gas* **2012**, *24*, 1–7.

44. Shen, H.L.; Qu, H.J.; Zhang, Y.N.; He, Y.P.; Yang, D.S. Preliminary evaluation of the exploring potentially of the Beijiao Sag in the deep water area of the Qiongdongnan Basin. *Inn. Mong. Petrochem.* **2014**, *7*, 1–5.

45. Li, J.S.; Li, X.Q.; Wang, Y.; Wang, G.; Xu, X.D.; Liu, H.Y. Geochemical characteristics and hydrocarbon generation potential evaluation of source rocks in the deep water area of Qiongdongnan Basin. *J. Min. Sci. Technol.* **2021**, *6*, 166–175.

46. Gan, J.; Zhang, Y.Z.; Liang, G.; Yang, X.B.; Yang, J.H.; Li, X.; Guo, X.X. Research on Accumulation Process and Dynamic Mechanism of Natural Gas in the Deep Water Area of Central Canyon, Qiongdongnan Basin. *Earth Sci.* **2018**, *44*, 2627–2635.

47. Li, Y.; Wang, Z.S.; Shao, L.Y. Reservoir characteristics and formation model of Upper Carboniferous bauxite series in eastern Ordos Basin, NW China. *Pet. Explor. Dev.* **2024**, *51*, 1–9. [CrossRef]

48. Tang, X.; Ripepi, N.; Stadie, P.N. A dual-site Langmuir equation for accurate estimation of high-pressure deep shale gas resources. *Fuel* **2016**, *185*, 10–17. [CrossRef]

49. Zhang, Y.Y.; Huang, Z.Q.; Zhao, F.; Yuan, G.X.; Wang, H.J.; Ran, T. Study on correlation between mineral composition and permeability characteristics of weathered granite. *J. North China Univ. Water Resour. Electr. Power (Nat. Sci. Ed.)* **2022**, *43*, 103–108.

50. Bellemans, F.; De, F.; Van, P. Composition of SRM and CN U-doped glasses: Significance for their use as thermal neutron fluence monitors in fission track dating. *Radiat. Meas.* **1995**, *24*, 153–160. [CrossRef]

51. Qu, H.Z.; Liu, M.Y.; Zhang, Y.F.; Wang, Z.Y.; Zhang, Z.H.; Li, S.Y.; Deng, X.L. Paleokarstic water table and their controlling on reservoirs in Ordovician Yingshan Formation, Tazhong Area, Tarim Basin, NW China. *Pet. Explor. Dev.* **2018**, *45*, 817–827. [CrossRef]

52. Hou, Z.S.; Zhou, L.H.; Chen, S.Y.; Pu, X.G.; Lou, D.; Fu, L.X. Reservoir types and controlling factors of Upper Paleozoic in Dagang exploration area. *J. China Univ. Min. Technol.* **2018**, *47*, 1021–1037.

53. Feng, Q.F.; Jiang, Q.C.; Ren, M.Y.; Wang, Z.C.; Liu, Y.M.; Tian, H.; Huang, S.P. A multi-well evaluation method for carbonate karst reservoirs and its geological application. *Nat. Gas Ind.* **2019**, *39*, 39–47.

54. Li, J.P.; Zhou, X.H.; Wang, G.Z. Lithologic constitution and its control on reservoir development on Penglai 9-1 buried hill, Bohai Sea Basin. *Earth Sci.* **2014**, *39*, 1521–1530.

55. Wang, D.Y.; Wang, Q.B.; Liu, X.J.; Zhao, M.; Hao, Y.W. Characteristics and developing patterns of gneiss buried hill weathering crust reservoir in the sea area of the Bohai Bay Basin. *Acta Petrol. Sin.* **2019**, *35*, 1181–1193.

56. Song, B.R.; Hu, Y.; Bian, S.Z.; Han, D.H.; Chui, X.D.; Zhang, J. Reservoir characteristics of the crystal basement in the Xinglongtai buried-hill, Liaohe Depression. *Acta Pet. Sin.* **2011**, *32*, 77–82.

57. Masao, S.; Takashi, O.; Masamichi, I. Nonoscale surface observation of feldspar dissolved under supercritical CO2-water-mineral system. *Energy*, 2005; 30, 2334–2343.

58. Zhou, X.H.; Xiang, H.; Yu, S.; Wang, G.; Yao, C.H. Reservoir characteristics and development controlling factors of JZS Neo Archean Metamporphic buried hill oil pool in Bohai Sea. *Pet. Explor. Dev.* **2005**, *32*, 17–20.

59. Li, B.J.; Yang, J.C.; Li, Y.L.; Tan, L.H.; Duan, F.J. Estimating ages of landforms by analyzing rock-weathering rinds. *Geogr. Res.* **1996**, *15*, 11–21.

60. Zou, C.N.; Hou, L.H.; Tao, S.Z.; Yuan, X.J.; Zhu, R.K.; Zhang, X.X.; Li, F.H.; Pang, Z.L. Hydrocarbon accumulation mechanism and structure of large-scale volcanic weathering crust of the Carboniferous in northern Xinjiang, China. *China Earth Sci.* **2011**, *41*, 1613–1626. [CrossRef]

61. Chen, X.M. Granite weathering profiles in the sea area of Guangdong and the analysis on features of differential weathering phenomenon. *Road Transp. Guangdong* **2003**, *1*, 59–64.

62. Sun, Q.F.; Colin, C.; Chen, F.H.; Zhang, J.W. A discussion on the factors affecting formation and quantity of clay minerals in climatic and environmental researches. *Acta Petrol. ET Mineral.* **2011**, *30*, 291–300.

63. Xie, J.Y.; Qin, J.G.; Li, J.; Cai, K.L.; Liu, X.Y. Palynological assemblages of the Oligocene in the Yinggehai-Qiongdongnan Basin of the northern South China Sea and their paleoenvironmental implications. *Acta Micropalaeontologica Sin.* **2014**, *31*, 85–97.

64. Zhang, Y.F.; Liu, D.S.; Zhang, X.H. Neogene palynological assemblages from Qiongdongnan Basin and their paleoclimate implications. *Mar. Geol. Quat. Geol.* **2017**, *37*, 93–101.

65. Han, C.C.; Tian, J.J.; Hu, C.L.; Liu, H.L.; Wang, W.F.; Huan, Z.P.; Feng, S. Lithofacies characteristics and their controlling effects on reservoirs in buried hills of metamorphic rocks: A case study of late Paleozoic units in the Aryskum depression, South Turgay Basin, Kazakhstan. *J. Pet. Sci. Eng.* **2020**, *191*, 107137. [CrossRef]

66. Zhang, L.P.; Yang, D.Y.; Zhu, D.K. Research on the weathering rate of crystallizine rock in a anticline of Yangtze River. *Sci. China (Ser. D)* **2003**, *33*, 81–88.

67. Zang, C.Y.; Zhang, T.Y.; Qu, R.T.; Zhang, X.D.; Yang, J.L.; Hao, P.; He, Y.J.; Song, X.Z. The Diagenesis characteristics of granitic buried-hill weathering crust reservoir in the sea area of Bohai. In Proceedings of the 17th Academic Conference Papers of Chinese Society for Mineralogy, Petrology and Geochemistry, Hangzhou, China, 19–22 April 2019.

68. Li, X.; Xie, Q.B.; Niu, H.P.; Zhang, Y.S.; Li, J.W.; Wu, Z.X.; Li, C.L.; Xi, B.; Wang, B.; Yuan, H.L. Main characteristics and evaluation of bedrock reservoirs in eastern segment of Altun Piedmont. *Earth Sci.* **2020**, *45*, 618–632.

69. Bai, B.; Wang, Q.B.; Zhao, G.X.; Liu, X.J. Cenozoic tectonic evolution of PL9-1 structure: An evidence of apatite fission track. *Acta Pet Sin.* **2015**, *36*, 1098–1108.

70. Li, S.B.; Wang, Y.J.; Wu, S.M. Meso-Cenozoic tectonothermal pattern of the Pearl Mouth Basin: Constraints from zircon and apatite fission track data. *Earth Sci. Front.* **2018**, *25*, 95–107.

71. Hu, S.B.; Long, Z.L.; Zhu, J.Z.; Hu, D.; Huang, Y.P.; Shi, Y.L.; Hu, J. Characteristics of geothermal field and the tectonic-thermal evolution in Pearl River Mouth Basin. *Acta Pet. Sin.* **2019**, *40*, 178–187.

72. Xie, J.L.; Huang, C.; Xiang, F.Y. Evolution of Cenozoic tectono- palaeogeography and its petroleum significance the western South China Sea. *Chin. J. Geol.* **2008**, *43*, 133–153.

73. Lv, B.F.; Yin, Z.X.; Cai, Z.R.; Wan, Z.F. Cenozoic tectonic evolution sequence in northern South China Sea and its oil/gas significance. *Acta Geol. Sin.* **2012**, *86*, 1249–1261.

74. Tian, L.X.; Wu, G.J.; Zhang, J.H. Formation of uplifts and sags in Miaoxi area of eastern Bohai Sea and their relationship with hydrocarbon accumulation. *Pet. Geol. Exp.* **2014**, *36*, 56–63.

75. Mao, J.R.; Li, Z.L.; Ye, H.M. Research on Mesozoic tectonic-magmatic activities in South China: Current situation and prospect. *Sci. China Earth Sci.* **2014**, *44*, 2593–2617.